

# Stability of the wobbling motion in an odd-mass nucleus and the analysis of $^{135}\text{Pr}$

Kosai Tanabe<sup>1</sup> and Kazuko Sugawara-Tanabe<sup>2,3</sup>

<sup>1</sup>*Department of Physics, Saitama University, Saitama City, Saitama 338-8570, Japan*

<sup>2</sup>*RIKEN Nishina Center, Wako, Saitama 351-0198, Japan*

<sup>3</sup>*Otsu Women's University, Sanbanyo 28-1, Chiyoda-ku, Tokyo 102-8357, Japan*

(Received 26 October 2016; revised manuscript received 6 April 2017; published 16 June 2017)

We apply alternative representations of Holstein-Primakoff boson expansion to the particle-rotor model as useful probes to test the stability and the physical contents of the exact solution. The diagonal representations with the total and single-particle angular momenta along the same axis (longitudinal case) and along two perpendicular axes (transverse case) are employed according to the system with rigid or hydrodynamical moments of inertia (MoI). The longitudinal case gives the normal wobbling mode for rigid MoI, but does not give a stable solution for hydrodynamical MoI. The transverse case applied for hydrodynamical MoI describes a few low spin states with reduced alignment of the total spin in the parallel direction to the single-particle spin, but these states differ from the wobbling mode which involves a quantized unit of rotational angular momentum. Employing the angular-momentum-dependent rigid MoI which is derived from the self-consistent Hartree-Fock-Bogoliubov equation together with angular momentum and particle-number constraints, we obtain good fitting not only to the energy-level scheme, but also to the electromagnetic transition rates and the mixing ratio for  $^{135}\text{Pr}$ .

DOI: 10.1103/PhysRevC.95.064315

## I. INTRODUCTION

Since wobbling motion was proposed by Bohr and Mottelson [1] as an indication of the triaxial rotor, there have been many experimental data to show the existence of the wobbling mode [2–8]. All the observed experimental data are around  $A \sim 160$  and limited to highly excited high spin states in odd-proton nuclei. The top-on-top model or the particle-rotor model with rigid (rig) moments of inertia (MoI) was successful in explaining not only the energy scheme but also the transition rates  $B(M1)$  and  $B(E2)$  in  $A \sim 160$  nuclei [9–12].

Recently, the transverse wobbling mode with hydrodynamical (hyd) MoI has been proposed for the yrast band near the ground state before the first backbending in  $^{135}\text{Pr}$  [13]. It is not yet verified whether the transverse wobbling mode exists, and Ref. [14] emphasizes the wobbling mode around the principal axis with the middle MoI. The wobbling mode for rotation around the axis with middle MoI never exists in the pure rotor model, as is proved in classical mechanics [15] and quantum mechanics [1] irrespective of rigid or hydrodynamical MoI. As for the particle-rotor model, as long as the rigid MoI is adopted, there is no chance to find wobbling around the axis with middle MoI, because the single-particle oscillator strength  $\omega_k$  [16] and the rigid MoI must both change their magnitudes as functions of  $\gamma$  in the same direction periodically with the same span of  $2\pi/3$ . However, the hydrodynamical MoI changes its magnitude in every span of  $\pi/3$  in an opposite direction to  $\omega_k$ , and so there may be a possibility to find the wobbling mode around the axis with middle MoI for the particle-rotor model with hydrodynamical MoI.

In the present paper, we extend the Holstein-Primakoff (HP) boson expansion method in the particle-rotor model with rigid MoI [9–12,17] to the case of hydrodynamical MoI. The extension of HP bosons to the odd- $A$  case introduces two kinds of bosons for the total angular momentum  $\vec{I}$  and the single-particle angular momentum  $\vec{j}$ . Thus, we can identify the nature of each band referring to two kinds of quantum numbers

$(n_\alpha, n_\beta)$  indicating the wobbling of  $\vec{I}$  and the precession of  $\vec{j}$ , respectively. In this scheme, both  $\vec{I}$  and  $\vec{j}$  interact on an equal footing. We make use of different choices of HP boson representations as theoretical probes of the physical contents of the exact results.

In Sec. II, we review the HP boson expansion method in odd- $A$  nuclei [9], where the stability equation is derived from the next-to-leading order in  $1/(2I)$  and  $1/(2j)$  together with the leading one. In order to clarify the meaning of quantum numbers, we discuss the special case when the single-particle potential vanishes. In Sec. III, the algebraic method is applied to the hydrodynamical MoI when the single-particle potential exists. In Sec. III B, we investigate the transverse case by applying the diagonal HP boson representation for  $I_y$  and  $j_x$ . We discuss the results of this analysis in detail. In Sec. IV, the particle-rotor model with angular-momentum-dependent ( $I$ -dependent) rigid MoI, which is derived from the self-consistent constrained Hartree-Fock-Bogoliubov (HFB) equations [18], is applied to reproduce the experimental data in  $^{135}\text{Pr}$  [13,19]. In Sec. V, the paper is summarized and concluded.

## II. HOLSTEIN-PRIMAKOFF BOSON EXPANSION METHOD

### A. Top-on-top model (particle-rotor model)

We adopt the particle-rotor Hamiltonian given by

$$H = H_{\text{rot}} + H_{\text{sp}} \quad (1)$$

with

$$H_{\text{rot}} = \sum_{k=x,y,z} A_k (I_k - j_k)^2, \quad (2a)$$

$$H_{\text{sp}} = \frac{V}{j(j+1)} [\cos \gamma (3j_z^2 - \vec{j}^2) - \sqrt{3} \sin \gamma (j_x^2 - j_y^2)], \quad (2b)$$

where  $\vec{I}$  is the total angular momentum,  $\vec{j}$  the single-particle angular momentum,  $A_k = 1/(2\mathcal{J}_k)$  for MoI  $\mathcal{J}_k$  ( $k = 1, 2, 3$  or  $x, y, z$ ), and the deformation parameters describing the ellipsoidal shape of the rotor are  $\beta_2$  and  $\gamma$ .

Here we remark that  $H_{\text{sp}}$  is derived from the  $\gamma$ -deformed Nilsson potential [16]

$$H_\delta = -\hbar\omega_0(\delta)\beta_2 r^2 \left[ \cos \gamma Y_{20} - \frac{1}{2} \sin \gamma (Y_{22} + Y_{2-2}) \right] \quad (3)$$

by applying the Wigner-Eckart theorem for the single- $j$  case:

$$\begin{aligned} \langle jm | r^2 \left[ \cos \gamma Y_{20} - \frac{1}{2} \sin \gamma (Y_{22} + Y_{2-2}) \right] | jm \rangle \\ = -\frac{1}{8j(j+1)} \sqrt{\frac{5}{\pi}} \langle jm | r^2 \left[ \cos \gamma (3j_z^2 - \vec{j}^2) \right. \\ \left. - \sqrt{3} \sin \gamma (j_x^2 - j_y^2) \right] | jm \rangle. \end{aligned} \quad (4)$$

Comparing Eq. (2b) with Eqs. (3) and (4),  $V$  is related to the  $\gamma$ -deformed Nilsson potential as

$$V = \frac{1}{8} \sqrt{\frac{5}{\pi}} \hbar\omega_0(\delta) \beta_2 \langle r^2 \rangle_{jm}. \quad (5)$$

Then, for the  $h_{11/2}$  orbital and  $\beta_2 = 0.18$  which is adopted in Ref. [13] for the  $^{135}\text{Pr}$  nucleus,  $V$  is almost equal to 1.5 MeV, if we choose  $\langle r^2 \rangle_{jm} = N + 3/2$  as in Ref. [16]. To enhance the effect of  $V$  we choose  $V = 1.6$  MeV in this paper.

We study two models for  $\mathcal{J}_k$ , the hydrodynamical model in Lund convention,

$$\mathcal{J}_k^{\text{hyd}} = \frac{4}{3} \mathcal{J}_0 \sin^2 \left( \gamma + \frac{2}{3} \pi k \right), \quad (6a)$$

and the rigid-body model in Lund convention,

$$\mathcal{J}_k^{\text{rig}} = \frac{\mathcal{J}_0}{1 + \left( \frac{5}{16\pi} \right)^{1/2} \beta_2} \left[ 1 - \left( \frac{5}{4\pi} \right)^{1/2} \beta_2 \cos \left( \gamma + \frac{2}{3} \pi k \right) \right]. \quad (6b)$$

Note that the maximum rigid MoI is  $\mathcal{J}_x^{\text{rig}}$  with  $\mathcal{J}_x^{\text{rig}} \geq \mathcal{J}_y^{\text{rig}} \geq \mathcal{J}_z^{\text{rig}}$  in  $0 \leq \gamma \leq \pi/3$ . As seen in Eqs. (2b) and (6b), there is no possibility to find the transverse wobbling because both the coefficient of  $j_k^2$  in  $H_{\text{sp}}$  and  $1/\mathcal{J}_k^{\text{rig}}$  increase or decrease in the same direction as functions of  $\gamma$  with the same periodicity. Both are derived from the radius,

$$r_k = R_0 \left[ 1 + \left( \frac{5}{4\pi} \right)^{1/2} \beta_2 \cos \left( \gamma + \frac{2\pi k}{3} \right) \right]. \quad (7)$$

However,  $1/\mathcal{J}_k^{\text{hyd}}$  changes in the opposite direction with a different periodicity as a function of  $\gamma$ , compared to the coefficient of  $j_k^2$  in  $H_{\text{sp}}$ . Then, there may occur a possibility to find the transverse wobbling mode.

The rotor Hamiltonian is invariant with respect to rotation through an angle  $\pi$  about each of three principal axes,  $\mathcal{R}_k(\pi) = \exp(-i\pi R_k)$  with  $R_k = I_k - j_k$  ( $k = 1, 2, 3$ ). These symmetry operations compose the  $D_2$  symmetry group, which has four representations labeled by  $(r_1, r_2, r_3)$ , where  $r_k$  stands for an eigenvalue of  $\mathcal{R}_k(\pi)$  and takes the value  $+1$  or  $-1$ , and  $r_1 r_2 r_3 = 1$  [1]. Bohr symmetry [20] requires that only the

states belonging to the  $(r_1, r_2, r_3) = (+1, +1, +1)$  representation are allowed as nuclear states, unless the corresponding invariance of the Hamiltonian is violated for some reason. We refer to both  $D_2$  symmetry and Bohr symmetry simply as  $D_2$  invariance, hereafter. If the  $x$  axis is chosen as the quantization axis, the physical states must be invariant under both operations  $\mathcal{R}_3(\pi) = \exp\{-i\pi(I_z - j_z)\}$  and  $\mathcal{R}_1(\pi) = \exp\{-i\pi(I_x - j_x)\}$ . A complete set of the  $D_2$ -invariant basis states is provided by

$$\begin{aligned} \left\{ \sqrt{\frac{2I+1}{16\pi^2}} [\mathcal{D}_{MK'}^I(\theta_i) \phi_{\Omega'}^j + (-1)^{I-j} \mathcal{D}_{M-K'}^I(\theta_i) \phi_{-\Omega'}^j]; \right. \\ \left. |K' - \Omega'| = \text{even}, \quad \Omega' > 0 \right\}, \end{aligned} \quad (8)$$

where  $\phi_{\Omega'}^j$  stands for the single-particle state, and  $\mathcal{D}_{MK'}^I(\theta_i)$  for the Wigner  $\mathcal{D}$  functions.

From now on we discuss the case of  $I \geq j$ . Because the magnitude  $R$  of the rotor angular momentum  $\vec{R} = \vec{I} + (-\vec{j})$  is given by  $R = I - j, I - j + 1, \dots, I + j - 1$ , or  $I + j$ , an integer  $n_{\beta'}$  defined by  $R = I - j + n_{\beta'}$  takes the values

$$n_{\beta'} = 0, 1, 2, \dots, 2j. \quad (9)$$

As  $R_x$  runs from  $R$  to  $-R$ , and  $R_x = I_x - j_x = K' - \Omega' = \text{even}$ , an integer  $n_{\alpha'}$  defined by the relation  $R_x = R - n_{\alpha'}$  takes the values

$$\begin{aligned} n_{\alpha'} = 0, 2, 4, \dots, 2R, \quad \text{for } R = \text{even}, \\ n_{\alpha'} = 1, 3, 5, \dots, 2R - 1, \quad \text{for } R = \text{odd}. \end{aligned} \quad (10)$$

Physical states are realized for a set of non-negative integers  $n_{\alpha'}$  and  $n_{\beta'}$ , which are related to the magnitude of rotor angular momentum  $R$  and its  $x$  component  $R_x$  through the relations  $R = I - j + n_{\beta'}$  and  $R_x = I - j + n_{\beta'} - n_{\alpha'}$  by the  $D_2$ -invariance rule. When we consider the  $y$  axis as the quantization axis,  $R_y = I - j + n_{\beta'} - n_{\alpha'}$  by the  $D_2$ -invariance rule. We diagonalize Eq. (1) within the  $D_2$ -invariant basis Eq. (8) to obtain the exact solution.

## B. Diagonal boson representation for both $\vec{I}$ and $\vec{j}$ in the same direction

At first, we consider the HP boson expansion method for the system with rigid MoI, which explains both the energy levels and the in-band and out-of-band transition rates  $B(E2)$  and  $B(M1)$  in Lu isotopes [9–12]. Because the coefficient of  $I_x^2$  and also the coefficient of  $j_x^2$  are the smallest among the other coefficients in Eqs. (2a) and (2b), it is expected that the total energy becomes the lowest when both angular momentum vectors  $\vec{I}$  and  $\vec{j}$  are aligned along the  $x$  direction. Therefore, we choose the diagonal forms for the components  $I_x$  and  $j_x$  in the HP boson representation as follows:

$$\begin{aligned} I_+ &= I_-^\dagger = I_y + iI_z = -\hat{a}^\dagger \sqrt{2I - \hat{n}_a}, \\ I_x &= I - \hat{n}_a, \quad \text{with } \hat{n}_a = \hat{a}^\dagger \hat{a}, \\ j_+ &= j_-^\dagger = j_y + ij_z = \sqrt{2j - \hat{n}_b} \hat{b}, \\ j_x &= j - \hat{n}_b \quad \text{with } \hat{n}_b = \hat{b}^\dagger \hat{b}. \end{aligned} \quad (11)$$

Using these representations, we rewrite Hamiltonian (1) in terms of two kinds of boson operators,  $\hat{a}$  and  $\hat{b}$ . Here we note that  $I_k$  satisfies commutation relations with a minus sign, while  $j_k$  satisfies normal commutation relations [21]:

$$[I_i, I_j] = -iI_{i \times j}, [j_i, j_j] = ij_{i \times j}. \quad (12)$$

For the system with hydrodynamical MoI, where  $\mathcal{J}_y^{\text{hyd}} > \mathcal{J}_x^{\text{hyd}} > \mathcal{J}_z^{\text{hyd}}$ , another boson representation is preferable:

$$\begin{aligned} I_+ &= I_-^\dagger = I_z + iI_x = -\hat{a}^\dagger \sqrt{2I - \hat{n}_a}, \\ I_y &= I - \hat{n}_a, \quad \text{with } \hat{n}_a = \hat{a}^\dagger \hat{a}; \\ j_+ &= j_-^\dagger = j_z + ij_x = \sqrt{2j - \hat{n}_b} \hat{b}, \\ j_y &= j - \hat{n}_b, \quad \text{with } \hat{n}_b = \hat{b}^\dagger \hat{b}. \end{aligned} \quad (13)$$

Similarly, for the region where  $\gamma \sim 0$  but  $\neq 0$ , the following representation is preferable [17]:

$$\begin{aligned} I_+ &= I_-^\dagger = I_x + iI_y = -\hat{a}^\dagger \sqrt{2I - \hat{n}_a}, \\ I_z &= I - \hat{n}_a, \quad \text{with } \hat{n}_a = \hat{a}^\dagger \hat{a}; \\ j_+ &= j_-^\dagger = j_x + ij_y = \sqrt{2j - \hat{n}_b} \hat{b}, \\ j_z &= j - \hat{n}_b, \quad \text{with } \hat{n}_b = \hat{b}^\dagger \hat{b}. \end{aligned} \quad (14)$$

In any of Eqs. (11), (13), and (14), we expand the square roots  $\sqrt{2I - \hat{n}_a}$  and  $\sqrt{2j - \hat{n}_b}$  up to the order of  $\hat{n}_a/(2I)$  and  $\hat{n}_b/(2j)$  as small quantities:

$$\begin{aligned} \sqrt{2I - \hat{n}_a} &\cong \sqrt{2I} \left( 1 - \frac{\hat{n}_a}{4I} \right), \\ \sqrt{2j - \hat{n}_b} &\cong \sqrt{2j} \left( 1 - \frac{\hat{n}_b}{4j} \right). \end{aligned} \quad (15)$$

Then, the Hamiltonian contains the fourth order terms in boson operators in addition to the second order ones. For simplicity, we call this order of approximation next-to-leading order approximation, in contrast to the leading order approximation. The latter includes only the lowest order contributions from the expansion of Eq. (15), and the Hamiltonian includes contributions up to the terms bilinear in the boson operators.

Applying HP transformation of Eq. (11) to the Hamiltonian Eq. (1) with the rigid MoI Eq. (6b), we expand  $\sqrt{2I - \hat{n}_a}$  and  $\sqrt{2j - \hat{n}_b}$  into series in  $\hat{n}_a/(2I)$  and  $\hat{n}_b/(2j)$ , and retain up to the next-to-leading order. We arrive at an approximate Hamiltonian written in terms of two kinds of HP bosons

$$H_B \cong H_0 + H_2 + H_4, \quad (16)$$

where  $H_0$  denotes a constant which collects all the terms independent of boson operators,  $H_2$  the bilinear forms of boson operators, and  $H_4$  the fourth order terms. Their explicit forms are given by using  $A_k^{\text{rig}} = 1/(2\mathcal{J}_k^{\text{rig}})$  as

$$\begin{aligned} H_0 &= A_x^{\text{rig}}(I - j)^2 + \frac{1}{2}(A_y^{\text{rig}} + A_z^{\text{rig}} - 2A_x^{\text{rig}}) \\ &\quad - 2V \cos(\gamma - \pi/3) \left( 1 - \frac{3}{4j(j+1)} \right), \end{aligned} \quad (17)$$

$$H_2 = (\hat{a} \quad \hat{b} \quad \hat{a}^\dagger \quad \hat{b}^\dagger) \begin{pmatrix} A & G & B & F \\ G & C & F & D \\ B & F & A & G \\ F & D & G & C \end{pmatrix} \begin{pmatrix} \hat{a}^\dagger \\ \hat{b}^\dagger \\ \hat{a} \\ \hat{b} \end{pmatrix}, \quad (18)$$

where the coefficients are defined by

$$\begin{aligned} A &= \frac{1}{2} \left( I - \frac{1}{2} \right) A_{yzx} + j A_x^{\text{rig}}, \quad B = \frac{1}{2} \left( I - \frac{1}{4} \right) A_{yz}, \\ C &= \frac{1}{2} \left( j - \frac{1}{2} \right) a_{yzx} + I A_x^{\text{rig}}, \quad D = \frac{1}{2} \left( j - \frac{1}{4} \right) a_{yz}, \\ F &= \frac{1}{2} \sqrt{Ij} (A_y^{\text{rig}} + A_z^{\text{rig}}), \quad G = \frac{1}{2} \sqrt{Ij} A_{yz}, \\ A_{yzx} &= A_y^{\text{rig}} + A_z^{\text{rig}} - 2A_x^{\text{rig}}, \quad A_{yz} = A_y^{\text{rig}} - A_z^{\text{rig}}, \\ a_{yz} &= A_{yz} + \frac{2\sqrt{3}V}{j(j+1)} \sin(\gamma - \pi/3), \\ a_{yzx} &= A_{yzx} + \frac{6V}{j(j+1)} \cos(\gamma - \pi/3). \end{aligned} \quad (19)$$

To diagonalize  $H_2$  in Eq. (18), we solve the eigenvalue equation taking account of the metric arising from the boson commutation relation:

$$\begin{vmatrix} A - \omega & G & B & F \\ G & C - \omega & F & D \\ -B & -F & -A - \omega & -G \\ -F & -D & -G & -C - \omega \end{vmatrix} = 0. \quad (20)$$

This equation reduces to

$$\omega^4 - b\omega^2 + c = 0, \quad (21)$$

with

$$\begin{aligned} b &\equiv A^2 - B^2 + C^2 - D^2 + 2(G^2 - F^2), \\ c &\equiv (A^2 - B^2)(C^2 - D^2) + (G^2 - F^2)^2 \\ &\quad + 4FG(AD + BC) - 2(AC + BD)(F^2 + G^2). \end{aligned} \quad (22)$$

Equation (21) gives two positive solutions

$$2\omega_{(\pm)}^2 = b \pm \sqrt{b^2 - 4c}, \quad (23)$$

only when

$$b^2 - 4c \geq 0, \quad b > 0, \quad c > 0. \quad (24)$$

These inequalities compose the stability conditions for the wobbling mode and the precession mode [9].

The diagonalization of  $H_2$  given in Eq. (18) is attained by the unitary transformation (or the boson Bogoliubov transformation) connecting the boson operators  $(\hat{a}, \hat{b}, \hat{a}^\dagger, \hat{b}^\dagger)$  to the quasiboson operators  $(\alpha, \beta, \alpha^\dagger, \beta^\dagger)$ :

$$\begin{pmatrix} \hat{a} \\ \hat{b} \\ \hat{a}^\dagger \\ \hat{b}^\dagger \end{pmatrix} = \begin{pmatrix} u_+ & w_+ & u_-^* & w_-^* \\ v_+ & t_+ & v_-^* & t_-^* \\ u_- & w_- & u_+^* & w_+^* \\ v_- & t_- & v_+^* & t_+^* \end{pmatrix} \begin{pmatrix} \alpha \\ \beta \\ \alpha^\dagger \\ \beta^\dagger \end{pmatrix}. \quad (25)$$

The normalized column vectors in this transformation matrix are determined from the set of homogeneous equations

$$\begin{pmatrix} A & G & B & F \\ G & C & F & D \\ -B & -F & -A & -G \\ -F & -D & -G & -C \end{pmatrix} \begin{pmatrix} u_+ & w_+ & u_-^* & w_-^* \\ v_+ & t_+ & v_-^* & t_-^* \\ u_- & w_- & u_+^* & w_+^* \\ v_- & t_- & v_+^* & t_+^* \end{pmatrix} = \begin{pmatrix} u_+ & w_+ & u_-^* & w_-^* \\ v_+ & t_+ & v_-^* & t_-^* \\ u_- & w_- & u_+^* & w_+^* \\ v_- & t_- & v_+^* & t_+^* \end{pmatrix} \begin{pmatrix} \omega_\alpha & 0 & 0 & 0 \\ 0 & \omega_\beta & 0 & 0 \\ 0 & 0 & -\omega_\alpha & 0 \\ 0 & 0 & 0 & -\omega_\beta \end{pmatrix} \quad (26)$$

together with the orthonormality relations

$$\begin{aligned} |u_+|^2 - |u_-|^2 + |w_+|^2 - |w_-|^2 \\ = |v_+|^2 - |v_-|^2 + |t_+|^2 - |t_-|^2 = 1, \\ u_+v_-^* - u_-^*v_+ + w_+t_-^* - w_-^*t_+ \\ = u_+^*v_- - u_-v_+^* + w_+^*t_- - w_-t_+^* = 0, \\ |u_+|^2 - |u_-|^2 + |v_+|^2 - |v_-|^2 \\ = |w_+|^2 - |w_-|^2 + |t_+|^2 - |t_-|^2 = 1, \\ u_+^*w_- - u_-^*w_+ + v_+^*t_- - v_-^*t_+ \\ = u_+w_-^* - u_-w_+^* + v_+t_-^* - v_-t_+^* = 0. \end{aligned} \quad (27)$$

Here, we can take real solutions for the coefficients of quasibosons in Eq. (25). In Eq. (26),  $\omega_\alpha$  or  $\omega_\beta$  corresponds to either of  $\omega_{(\pm)}$  ( $\omega_{(+)} > \omega_{(-)}$ ). In Ref. [9], Eq. (26) is solved in two steps. At first, the dangerous terms  $\hat{a}^\dagger \hat{a}^\dagger + \text{H.c.}$  and  $\hat{b}^\dagger \hat{b}^\dagger + \text{H.c.}$  are eliminated without mixing  $\hat{a}$  and  $\hat{b}$ . Next, the remaining terms from  $\hat{a}^\dagger \hat{a}$ ,  $\hat{b}^\dagger \hat{b}$ , and  $\hat{a} \hat{b}$ ,  $\hat{a}^\dagger \hat{b}$  and their Hermitian conjugate terms are diagonalized. In the first step, we get

$$\begin{aligned} P_+ &= \left[ \frac{1}{2} \left( \frac{|A|}{\sqrt{A^2 - B^2}} + 1 \right) \right]^{1/2}, \\ P_- &= -\frac{AB}{|AB|} \left[ \frac{1}{2} \left( \frac{|A|}{\sqrt{A^2 - B^2}} - 1 \right) \right]^{1/2}, \\ Q_+ &= \left[ \frac{1}{2} \left( \frac{|C|}{\sqrt{C^2 - D^2}} + 1 \right) \right]^{1/2}, \\ Q_- &= -\frac{CD}{|CD|} \left[ \frac{1}{2} \left( \frac{|C|}{\sqrt{C^2 - D^2}} - 1 \right) \right]^{1/2}. \end{aligned} \quad (28)$$

Equation (31) in Ref. [9] works for rigid MoI in the range  $0^\circ < \gamma \leq 60^\circ$ , and also for hydrodynamical MoI defined by Eq. (3a) in Ref. [9] in the range  $0 < \gamma \leq 30^\circ$ , because  $A$  and  $C$  are positive and  $B$  and  $D$  are negative in these regions. However, for the general case Eq. (31) in Ref. [9] should be replaced by Eq. (28) in the present paper. There are two misprints in Ref. [9]: Eq. (38) should read

$$\beta = w_+ \hat{a} + t_+ \hat{b} - w_- \hat{a}^\dagger - t_- \hat{b}^\dagger, \quad (29)$$

and  $\text{sign}(p - q)$  in Eq. (44c) should read  $\text{sign}(q - p)$ . We comment that Eq. (44c) of Ref. [9] was obtained in the leading order approximation with  $V = 0$ . Although Ref. [9] solved Eq. (26) in two steps, it is also solvable directly in one step.

As long as the stability conditions in Eq. (24) are satisfied,  $H_2$  is diagonalized as

$$H_2 \simeq 2\omega_\alpha(\hat{n}_\alpha + 1/2) + 2\omega_\beta(\hat{n}_\beta + 1/2), \quad (30)$$

where we introduce number operators in the new quasiboson picture:

$$\hat{n}_\alpha = \alpha^\dagger \alpha \quad \text{and} \quad \hat{n}_\beta = \beta^\dagger \beta. \quad (31)$$

To take account of higher order terms, we apply the boson transformation to  $H_4$  and retain only diagonal terms which are expressed in terms of  $\hat{n}_\alpha$  and  $\hat{n}_\beta$ . Consequently, we arrive at an approximate formula for  $H_B$  as

$$\begin{aligned} H_B \simeq H_0 + \omega_\alpha + \omega_\beta + C_0 + (2\omega_\alpha + C_\alpha)\hat{n}_\alpha \\ + (2\omega_\beta + C_\beta)\hat{n}_\beta + C_{\alpha\alpha}\hat{n}_\alpha^2 + C_{\beta\beta}\hat{n}_\beta^2 + C_{\alpha\beta}\hat{n}_\alpha\hat{n}_\beta, \end{aligned} \quad (32)$$

where the six  $C$ 's are constants which arise from additional higher order terms describing the anharmonicity effect, and their explicit forms are listed in Ref. [9].

To clarify the physical meaning of the two quantum numbers  $n_\alpha$  and  $n_\beta$ , which are the eigenvalues of  $\hat{n}_\alpha$  and  $\hat{n}_\beta$ , we consider the pure rotor case, i.e.,  $V = 0$  in Eq. (1). Then, formula (32) reduces to a simple expression of the rotational energy:

$$\begin{aligned} E_{\text{rot}} \simeq A_x^{\text{rig}} R(R+1) - \frac{p+q}{2} n_\alpha^2 \\ + \left( 2R\sqrt{pq} + \sqrt{pq} - \frac{p+q}{2} \right) \left( n_\alpha + \frac{1}{2} \right), \end{aligned} \quad (33)$$

where

$$\begin{aligned} R = I - j + n_\beta, \quad R_x = R - n_\alpha, \\ p = A_y^{\text{rig}} - A_x^{\text{rig}}, \quad q = A_z^{\text{rig}} - A_x^{\text{rig}}. \end{aligned} \quad (34)$$

In the symmetric limit of  $A_y^{\text{rig}} = A_z^{\text{rig}}$  ( $\gamma = 60^\circ$ ), formula (33) becomes the well-known expression

$$E_{\text{rot}} = A_z^{\text{rig}} R(R+1) - (A_z^{\text{rig}} - A_x^{\text{rig}})(R - n_\alpha)^2. \quad (35)$$

The eigenvalue  $R$  can be regarded as an effective magnitude of the rotor angular momentum, and  $R - n_\alpha$  as its  $x$  component  $R_x$ . It turns out that these  $n_\alpha$  and  $n_\beta$  are the same integers  $n_{\alpha'}$  and  $n_{\beta'}$  as defined in Eqs. (9) and (10). This allows us to interpret the quantum number  $n_\alpha$  as the wobbling quantum number of  $\vec{R}$  [1] because of  $R_x = R - n_\alpha$ . The other quantum number  $n_\beta$  is interpreted as the precession of  $\vec{j}$ . In Eq. (33), if we stay in the leading order approximation, two wobbling energies reduce to

$$\omega_\alpha \sim (I - j)\sqrt{pq}, \quad \omega_\beta \sim (I - j)A_x^{\text{rig}}. \quad (36)$$

The wobbling energy  $\omega_\alpha$  becomes the same as Bohr and Mottelson's formula [1] with  $I - j$  instead of  $I$ . This result is also obtained from the leading order stability equation with  $V = 0$ , where the numbers  $-1/2$  and  $-1/4$  inside the factors like  $(I - 1/2)$  appearing in  $A$ ,  $B$ ,  $C$ , and  $D$  in Eq. (19) are

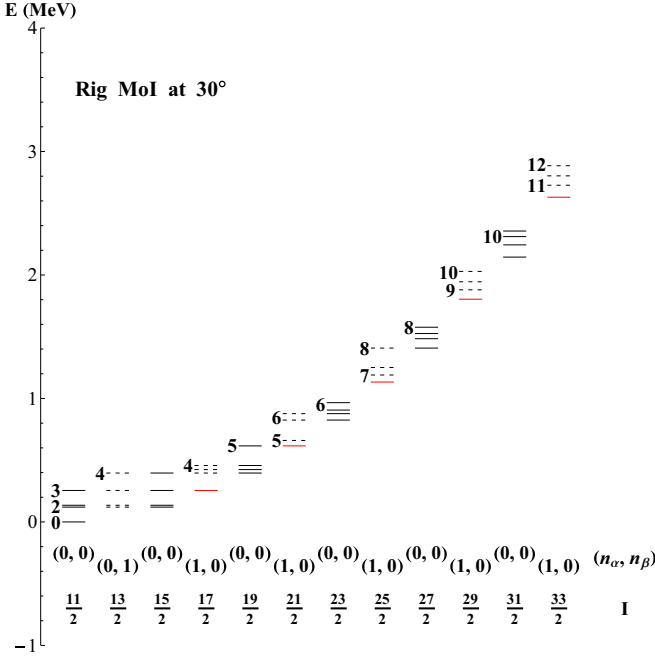


FIG. 1. The energy levels given by Eq. (33) for the rigid (rig) MoI at  $\gamma = 30^\circ$  as functions of  $I$ . The solid lines correspond to the levels with  $I - j = \text{even}$ , while the dashed lines and the lowest solid lines correspond to the ones with  $I - j = \text{odd}$ . A numeral beside each line denotes the value of  $R$ . A pair of quantum numbers  $(n_\alpha, n_\beta)$  next to the bottom is assigned to the yrast for each  $I$ . The lowest solid lines represent  $(1,0)$  for the yrast levels of  $I - j = \text{odd}$  for  $I \geq 17/2$ . The parameters are  $\mathcal{J}_0 = 25 \text{ MeV}^{-1}$  and  $\beta_2 = 0.18$ .

dropped. Then,

$$2\omega_{(\pm)}^2 = (I - j)^2 [pq + (A_x^{\text{rig}})^2 \pm |pq - (A_x^{\text{rig}})^2|]. \quad (37)$$

For the case of rigid MoI,  $pq - (A_x^{\text{rig}})^2$  is always negative in the region  $0^\circ \leq \gamma \leq 60^\circ$ . Thus, we get  $\omega_{(-)} = (I - j)\sqrt{pq} = \omega_\alpha$  and  $\omega_{(+)} = (I - j)A_x^{\text{rig}} = \omega_\beta$ , indicating that the lowest mode is the wobbling motion around the axis with the maximum MoI.

In Fig. 1, we show four energy levels from the yrast with  $\mathcal{J}_0 = 25 \text{ MeV}^{-1}$ ,  $\gamma = 30^\circ$ , and  $\beta_2 = 0.18$  in Eq. (6b). We choose  $j = 11/2$  in this paper. As seen in Fig. 1, the lowest energy in the band with  $I - j = \text{odd}$  shown by the solid lines is always  $(n_\alpha, n_\beta) = (1,0)$  except for  $I = 13/2$ , where  $(0,1)$  becomes lowest. Because of  $D_2$  invariance,  $R = 1$  is not allowed; subsequently no  $(1,0)$  case exists for  $I = 13/2$ . This is also found in the experimental data of Ref. [13]; i.e., no  $13/2$  level has been observed in the wobbling band. From the quantum numbers  $(1,0)$ , all the lowest levels in  $I - j = \text{odd}$  bands are wobbling modes around the  $x$  axis with the maximum MoI, except for the  $13/2$  level where the lowest level is the precession mode of  $j$  around the axis with maximum MoI. The energy levels are in good agreement with the exact results. Moreover, all these four levels from the yrast are well described by  $(n_\alpha, n_\beta)$ .

For the case of hydrodynamical MoI and  $V = 0$ , where  $\mathcal{J}_y^{\text{hyd}} > \mathcal{J}_x^{\text{hyd}} > \mathcal{J}_z^{\text{hyd}}$  in the region  $0^\circ \leq \gamma \leq 30^\circ$ , we apply

Eq. (13) to Eq. (2a) in the same approximation as Eq. (33), and get

$$E_{\text{rot}} \cong A_y^{\text{hyd}} R(R + 1) - \frac{p' + q'}{2} n_\alpha^2 + \left( 2R\sqrt{p'q'} + \sqrt{p'q'} - \frac{p' + q'}{2} \right) \left( n_\alpha + \frac{1}{2} \right), \quad (38)$$

where

$$R = I - j + n_\beta, \quad R_y = R - n_\alpha, \quad (39)$$

$$p' = A_z^{\text{hyd}} - A_y^{\text{hyd}}, \quad q' = A_x^{\text{hyd}} - A_y^{\text{hyd}}.$$

In the leading order approximation, Eq. (38) reduces to  $\omega_\alpha \sim (I - j)\sqrt{p'q'}$ , which is nothing but the wobbling mode around the axis with the maximum MoI  $\mathcal{J}_y^{\text{hyd}}$ , and to  $\omega_\beta \sim (I - j)A_y^{\text{hyd}}$ , the precession of  $j$  around the same axis. From Eq. (23) in the leading order approximation with  $V = 0$ , replacing  $(\mathcal{J}_x^{\text{rig}}, \mathcal{J}_y^{\text{rig}}, \mathcal{J}_z^{\text{rig}})$  by  $(\mathcal{J}_y^{\text{hyd}}, \mathcal{J}_z^{\text{hyd}}, \mathcal{J}_x^{\text{hyd}})$ , we get for hydrodynamical MoI

$$2\omega_{(\pm)}^2 = (I - j)^2 [p'q' + (A_y^{\text{hyd}})^2 \pm |p'q' - (A_y^{\text{hyd}})^2|]. \quad (40)$$

In the region  $0^\circ < \gamma \leq 30^\circ$ ,  $p'q' - (A_y^{\text{hyd}})^2$  is always positive, so that  $\omega_{(-)} = \omega_\beta$  and  $\omega_{(+)} = \omega_\alpha$ . Subsequently, the lowest mode is the precession of  $j$  around the axis with maximum MoI  $\mathcal{J}_y^{\text{hyd}}$ . In Fig. 2, we show four energy levels from the yrast

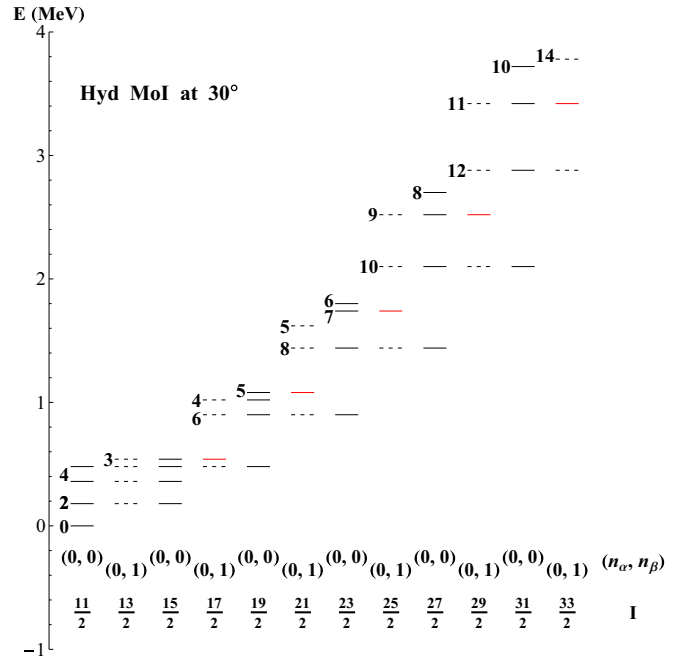


FIG. 2. The energy levels given by Eq. (38) for the hydrodynamical (hyd) MoI at  $\gamma = 30^\circ$  as functions of  $I$ . The solid lines correspond to the levels with  $I - j = \text{even}$ , while the dashed lines and the second solid lines correspond to the ones with  $I - j = \text{odd}$ . A numeral beside each line denotes the value of  $R$ . A pair of quantum numbers  $(n_\alpha, n_\beta)$  next to the bottom is assigned to the yrast for each  $I$ . The solid lines for the yrast levels with  $I \geq 17/2$  represent  $(1,0)$ . The parameter  $\mathcal{J}_0 = 25 \text{ MeV}^{-1}$  is the same as in Fig. 1.



with the same parameter as in Fig. 1. The energy levels from Eq. (38) coincide with the exact results because  $\gamma = 30^\circ$ . In contrast to Fig. 1, the lowest energy level in the band with  $I - j = \text{odd}$  is always labeled  $(n_\alpha, n_\beta) = (0, 1)$ , which is the precession mode of  $\vec{j}$  around the axis with the maximum MoI  $\mathcal{J}_y^{\text{hyd}}$ . There is no difference in  $(n_\alpha, n_\beta)$  between the  $I = 13/2$  level and the other levels with  $I - j = \text{odd}$ . This contradicts the non-observation of the  $I = 13/2$  level in Ref. [13]. The levels corresponding to the wobbling mode around the axis with the maximum MoI  $\mathcal{J}_y^{\text{hyd}}$ , i.e., the levels with  $(1, 0)$  (shown by solid lines), become the second lowest levels, which are represented by solid lines in Fig. 2. Not only the yrast levels but also all the other levels are well explained by  $(n_\alpha, n_\beta)$ .

For small  $\gamma$  ( $A_x \sim A_y$ ), the diagonal representation for both  $I_z$  and  $j_z$  in Eq. (14) is suitable. We have

$$E_{\text{rot}} \cong A_z R(R+1) + \frac{p'' + q''}{2} n_\alpha^2 - \left( 2R\sqrt{p''q''} + \sqrt{p''q''} - \frac{p'' + q''}{2} \right) \left( n_\alpha + \frac{1}{2} \right), \quad (41)$$

where

$$R = I - j + n_\beta, \quad R_z = R - n_\alpha, \quad (42)$$

$$p'' = A_z - A_x, \quad q'' = A_z - A_y.$$

In the symmetric limit of  $\gamma = 0^\circ$ , Eq. (41) goes to the well-known expression

$$E_{\text{rot}} = A_x R(R+1) - (A_x - A_z)(R - n_\alpha)^2, \quad (43)$$

though  $A_z^{\text{hyd}}$  diverges in this limit. The integer  $R$  can be regarded as an effective magnitude of the rotor angular momentum, and  $R - n_\alpha$  as its  $z$  component  $R_z$ . In Fig. 3, we show the energy levels for the hydrodynamical MoI at  $\gamma = 6^\circ$  with the same value of  $\mathcal{J}_0$  as in Fig. 2. A pair of numerals below now stands for  $(R, R_z)$ , and all the yrast levels have  $R_z = 0$ . Here we comment that Eq. (41) is easily obtained by replacing  $I$  and  $\tilde{k}$  in Eq. (7) of Ref. [17] by  $R$  and  $n_\alpha$ , respectively. Reference [17] is the first paper that applied the HP boson transformation to the triaxial rotor.

Similarly, in Fig. 4, we show the results for rigid MoI at  $\gamma = 6^\circ$  with the same parameters as in Fig. 1. A pair of numerals below stands for  $(R, R_z)$ , and all the yrast levels with  $I - j = \text{odd}$  have  $R_z = 2$ , except for  $I = 13/2$  where the  $R_z = 2$  level appears as the yrare levels. Once the  $D_2$  invariance is violated, the  $R_z = 2$  level splits into two levels characterized by  $(r_1, r_2, r_3) = (+1, +1, +1)$  and  $(+1, -1, -1)$  symmetry [1]. It may be a possible interpretation of the signature partner band reported in Ref. [13]. This is not realized with hydrodynamical MoI in Fig. 3, because  $R_z = 0$  does not split in both prolate and oblate sides even when the  $D_2$  invariance is violated (see Fig. 4-33 in Ref. [1]). The energy levels calculated from Eq. (41) reproduce the exact results, and not only the yrast but also all the other levels in Figs. 3 and 4 are well described by  $(R, R_z)$ .

To clarify the character of  $(0, 1)$  and  $(1, 0)$  levels, we show the alignments of  $\langle I_x^2 \rangle^{1/2}$  and  $\langle j_x^2 \rangle^{1/2}$  for the rigid MoI case

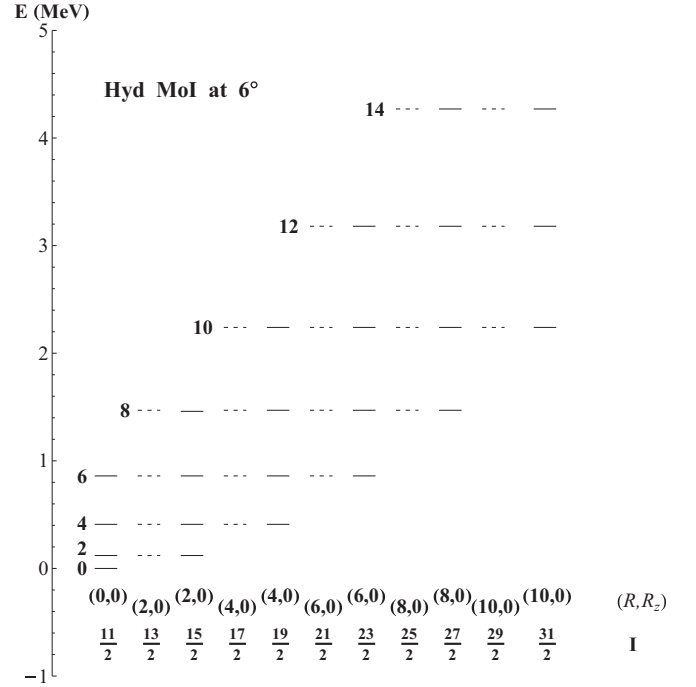


FIG. 3. The energy levels given by Eq. (41) for the hydrodynamical (hyd) MoI at  $\gamma = 6^\circ$  as functions of  $I$ . The solid lines correspond to the levels with  $I - j = \text{even}$ , while the dashed lines correspond to the levels with  $I - j = \text{odd}$ . A numeral beside each line denotes the value of  $R$ . A pair of quantum numbers  $(R, R_z)$  next to the bottom is assigned to the yrast for each  $I$ . The parameter set is the same as in Fig. 2.

in Fig. 5, and  $\langle I_y^2 \rangle^{1/2}$  and  $\langle j_y^2 \rangle^{1/2}$  for the hydrodynamical MoI case in Fig. 6, respectively. In both figures, the approximate solutions shown by open circles well overlap with the exact results shown by small solid circles. The approximate solutions are calculated using the wave functions directly obtained from the leading order approximation in Eq. (26). In Fig. 5,  $(n_\alpha, n_\beta) = (0, 0)$  is assigned to the  $I - j = \text{even}$  and  $(1, 0)$  to the  $I - j = \text{odd}$  case. In Fig. 6,  $(0, 0)$  is assigned to the  $I - j = \text{even}$ , and  $(0, 1)$  to the  $I - j = \text{odd}$  case. In both figures,  $I = 11/2$  and  $13/2$  are not shown, because  $b = c = 0$  for  $I = 11/2$  in the leading order approximation. As for  $I = 13/2$ , the value of  $\omega_{(-)}$  becomes quite small, indicating that the system is already close to the border of the stability domain. The agreement with the exact results is quite good in both figures, showing the usefulness of the HP boson method.

We investigate further details of Figs. 5 and 6. In Fig. 5, we find  $\langle I_x^2 \rangle_{I+2}^{1/2} - \langle I_x^2 \rangle_I^{1/2} \sim 2$  irrespective of whether  $I - j = \text{even}$  or odd. This regularity is also realized in the case with potential ( $V \neq 0$ ), as seen in Fig. 9. The unit 2 difference in  $\langle I_x^2 \rangle^{1/2}$  for  $\Delta I = 2$  indicates that the  $x$  axis plays the role of the quantization axis. The average values of  $\langle I_x^2 \rangle_{I+1}^{1/2} - \langle I_x^2 \rangle_I^{1/2}$  is  $-0.7$  for  $I - j = \text{even}$ , and  $2.7$  for  $I - j = \text{odd}$ , whose deviations from zero and 2 are related to the fluctuation of  $\langle j_x^2 \rangle^{1/2}$  between the solid and dashed lines. Because of  $V = 0$ , the staggering behavior of  $j_x$  is allowed, but  $I_x$  behaves to compensate such a fluctuation of  $j_x$  within a combination of  $A_x^{\text{rig}}(I_x - j_x)^2$  in  $H_{\text{rot}}$ . We confirm that the average value of

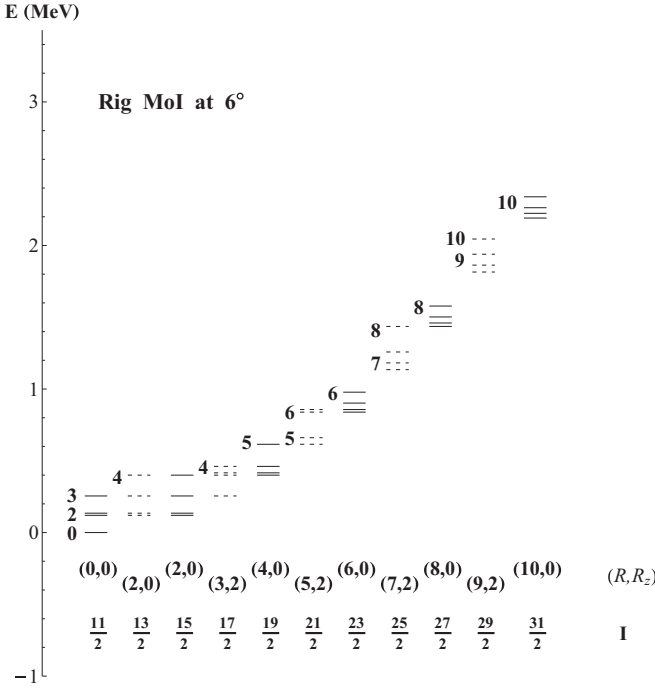


FIG. 4. The energy levels given by Eq. (41) for the rigid (rig) MoI at  $\gamma = 6^\circ$  as functions of  $I$ . The solid lines correspond to the levels with  $I - j = \text{even}$ , while the dashed lines correspond to the levels with  $I - j = \text{odd}$ . A numeral beside each line denotes the value of  $R$ . A pair of quantum numbers  $(R, R_z)$  next to the bottom is assigned to the yrast for each  $I$ . The parameter set is the same as in Fig. 1.

$(\langle I_x^2 \rangle^{1/2} - \langle j_x^2 \rangle^{1/2})_{I+1} - (\langle I_x^2 \rangle^{1/2} - \langle j_x^2 \rangle^{1/2})_I$  is  $-0.1$  for  $I - j = \text{even}$ , implying that  $\langle R_x^2 \rangle^{1/2}$  ( $R_x = I_x - j_x$ ) shows the stepwise behavior, which is quite similar to the one for the

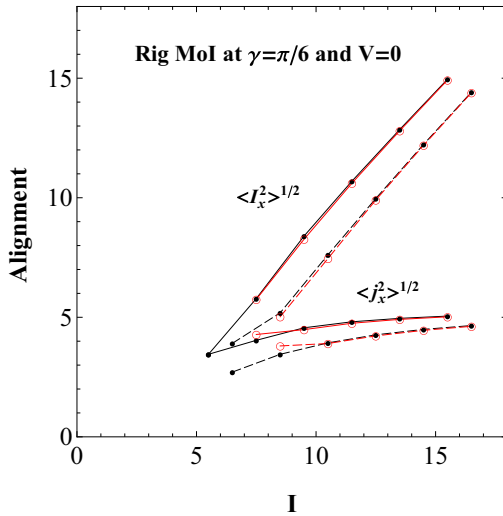


FIG. 5. Alignments of  $\langle I_x^2 \rangle^{1/2}$  and  $\langle j_x^2 \rangle^{1/2}$  for rigid (rig) MoI as functions of  $I$ . The solid circles connected by solid lines show exact results for  $I - j = \text{even}$  and the ones connected by dashed lines for  $I - j = \text{odd}$ . The open circles connected by solid and dashed lines show the corresponding results obtained from the leading order approximation. The parameter set is the same as in Fig. 1.

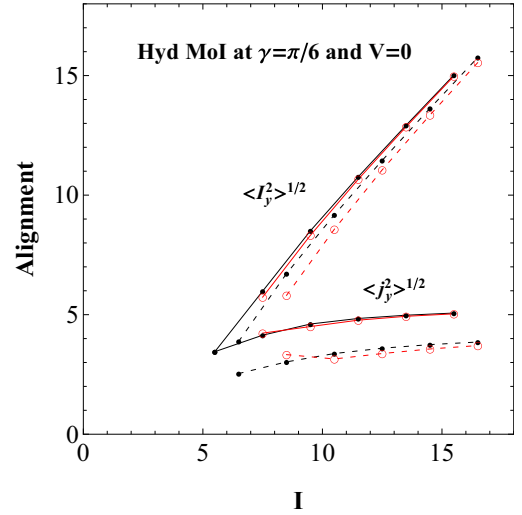


FIG. 6. Alignments of  $\langle I_y^2 \rangle^{1/2}$  and  $\langle j_y^2 \rangle^{1/2}$  for hydrodynamical (hyd) MoI as functions of  $I$ . The solid circles connected by solid lines show exact results for  $I - j = \text{even}$  and the ones connected by dashed lines for  $I - j = \text{odd}$ . The open circles connected by solid and dashed lines show the corresponding results obtained from the leading order approximation. The parameter set is the same as in Fig. 2.

$V \neq 0$  case [see Eqs. (62a) and (62b), and Fig. 15]. The average value of  $\frac{1}{2}(\langle I_x^2 \rangle_{I+2}^{1/2} + \langle I_x^2 \rangle_I^{1/2}) - \langle I_x^2 \rangle_I^{1/2}$  is almost 1 for  $I - j = \text{even}$ , which corresponds to the wobbling mode represented by the quantum number  $n_\alpha = 1$  (see Fig. 4(b) in Ref. [2]).

In Fig. 6, we find  $\langle I_y^2 \rangle_{I+2}^{1/2} - \langle I_y^2 \rangle_I^{1/2} \sim 2$  irrespective of whether  $I - j = \text{even}$  or odd. The unit 2 difference in  $\langle I_y^2 \rangle^{1/2}$  for  $\Delta I = 2$  indicates that the  $y$  axis plays the role of the quantization axis. We confirm that the average value of  $(\langle I_y^2 \rangle^{1/2} - \langle j_y^2 \rangle^{1/2})_{I+1} - (\langle I_y^2 \rangle^{1/2} - \langle j_y^2 \rangle^{1/2})_I$  is 0.1 for  $I - j = \text{odd}$ , implying that  $\langle R_y^2 \rangle^{1/2}$  ( $R_y = I_y - j_y$ ) shows the stepwise behavior like  $\langle R_y^2 \rangle_{I+2}^{1/2} - \langle R_y^2 \rangle_I^{1/2} = 2$ , and  $\langle R_y^2 \rangle_{I+1}^{1/2} = \langle R_y^2 \rangle_I^{1/2}$  for  $I - j = \text{odd}$ , in contrast to the rigid MoI case [see Eq. (62a)]. This coupling scheme corresponds to the cranking regime (see Fig. 4(a) in Ref. [2]). The average value of  $\frac{1}{2}(\langle j_y^2 \rangle_{I+2}^{1/2} + \langle j_y^2 \rangle_I^{1/2}) - \langle j_y^2 \rangle_{I+1}^{1/2}$  is assumed almost 1 for  $I - j = \text{even}$ , which is interpreted as the  $j$ -precession mode represented by the quantum number  $n_\beta = 1$  around the  $y$  axis with maximum MoI for the case of hydrodynamical MoI.

### III. HP BOSON EXPANSION METHOD APPLIED TO THE HYDRODYNAMICAL MOI CASE WITH $V \neq 0$

#### A. Diagonal boson representation for both $\vec{I}$ and $\vec{j}$ in the same direction (longitudinal case)

Now we discuss the case of  $V \neq 0$ . With some hope that  $\vec{j}$ , when pinned along the axis of medium MoI ( $x$  axis), may act to keep  $\vec{I}$  around the  $x$  axis through Coriolis force, we study the stability of the wobbling and the precessional motion of  $\vec{I}$  and  $\vec{j}$ . At first, we apply the same type of stability conditions as in Eqs. (22) and (24) obtained by replacing  $A^{\text{rig}}$ 's by  $A^{\text{hyd}}$ 's. Because of the relation  $\mathcal{J}_y^{\text{hyd}} > \mathcal{J}_x^{\text{hyd}} \geq \mathcal{J}_z^{\text{hyd}}$  for

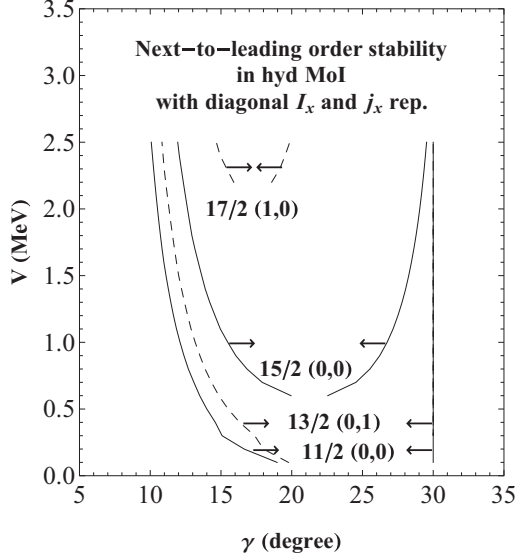


FIG. 7. Stability domain in the  $\gamma$ - $V$  plane for hydrodynamical (hyd) MoI with diagonal representation of  $I_x$  and  $j_x$  in the next-to-leading order approximation. The numerals denote the values of  $I$ . The solid lines are for the levels with  $I - j = \text{even}$ , while the dashed lines are for those with  $I - j = \text{odd}$ . The values of  $(n_\alpha, n_\beta)$  are shown for each  $I$ . The arrows attached to the lines indicate the region where the stability conditions are satisfied.

$5^\circ \leq \gamma \leq 30^\circ$ , the transverse wobbling may be realized when  $\vec{j}$  is aligned along the  $x$  axis. Equation (24) does not allow any stability region over the whole  $I$  range when  $V = 0$ , but once  $V > 0$  there appears some stability domain. In Fig. 7, we show the results with  $\mathcal{J}_0 = 25 \text{ MeV}^{-1}$ . The pattern of the diagram does not change for a different choice of  $\mathcal{J}_0$ , because the physical content depends only on the scaling factor  $s = \mathcal{J}_0 V$ . The levels with  $I = 11/2, 13/2$ , and  $15/2$  are stable in a finite range of  $\gamma$ , but the stability domain for the level with  $I = 17/2$  moves to the region of larger  $V$  ( $> 2.2 \text{ MeV}$ ) and narrow extent of  $\gamma$  about  $17^\circ$ . For the  $I = 19/2$  level the stability domain cannot be found within the region  $V \leq 6 \text{ MeV}$  and  $5^\circ \leq \gamma \leq 30^\circ$ . Moreover,  $(n_\alpha, n_\beta) = (0,0)$  is assigned to  $I = 11/2$  and  $I = 15/2$  levels, while  $(0,1)$  is assigned to the  $I = 13/2$  level. Thus, we do not find any stability region which allows the transverse wobbling for  $V \sim 1.5 \text{ MeV}$ .

We extend the stability analysis to the case with diagonal representation for both  $I_y$  and  $j_y$  as given by Eq. (13). The relevant quantities are obtained from Eq. (19) by replacing  $(\mathcal{J}_x^{\text{rig}}, \mathcal{J}_y^{\text{rig}}, \mathcal{J}_z^{\text{rig}})$  by  $(\mathcal{J}_x^{\text{hyd}}, \mathcal{J}_y^{\text{hyd}}, \mathcal{J}_z^{\text{hyd}})$ , and also  $\gamma - \pi/6$  by  $\gamma + \pi/6$ . From the results displayed in Fig. 8, we find that the stability domain is restricted to a quite narrow range in the  $\gamma$ - $V$  plane only for large  $I$ , i.e.,  $21/2 \leq I \leq 33/2$ . No stable region is found in the potential range of  $V \geq 0.3 \text{ MeV}$ .

We compare the exact results for the two models of rigid and hydrodynamical MoI. We show the calculated alignment of  $\vec{I}$  and  $\vec{j}$  along the  $x$  and  $y$  axes with rigid MoI in Fig. 9, and with hydrodynamical MoI in Fig. 10. The parameters are common for both models, i.e.,  $\mathcal{J}_0 = 25 \text{ MeV}^{-1}$ ,  $V = 1.6 \text{ MeV}$ ,  $\beta_2 = 0.18$ , and  $\gamma = 26^\circ$  as adopted in Ref. [13]. Figure 9 shows a typical example of wobbling mode. We confirm that

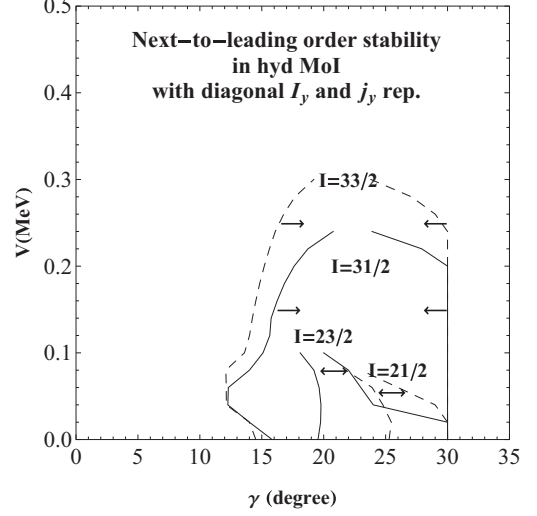


FIG. 8. Stability domain in the  $\gamma$ - $V$  plane for hydrodynamical (hyd) MoI with diagonal representation of  $I_y$  and  $j_y$  in the next-to-leading order approximation. The solid lines are for the levels with  $I - j = \text{even}$ , while the dashed lines are for those with  $I - j = \text{odd}$ . The arrows attached to the lines indicate the region where the stability conditions are satisfied.

$\langle I_x^2 \rangle_{I+2}^{1/2} - \langle I_x^2 \rangle_I^{1/2} = 2$  [2] and  $\langle I_x^2 \rangle_{I+1}^{1/2} - \langle I_x^2 \rangle_I^{1/2} = 0$  or  $2$  for  $I - j = \text{even}$  or  $\text{odd}$ , respectively. Therefore, the difference of  $\langle I_x^2 \rangle^{1/2}$  between the solid and dashed lines is almost one unit, while  $\langle j_x^2 \rangle^{1/2}$  and  $\langle j_y^2 \rangle^{1/2}$  are almost constant over the whole region of  $I$ . On the other hand, Fig. 10 shows that

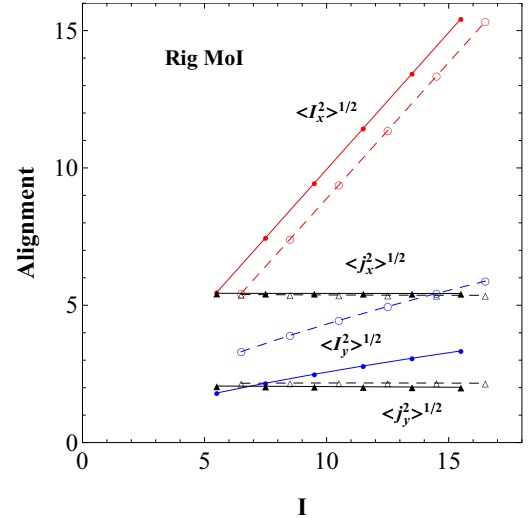


FIG. 9. The alignments of  $\langle I_x^2 \rangle^{1/2}$ ,  $\langle I_y^2 \rangle^{1/2}$ ,  $\langle j_x^2 \rangle^{1/2}$ , and  $\langle j_y^2 \rangle^{1/2}$  for the rigid (rig) MoI as functions of  $I$ . The solid circles connected by solid lines show  $\langle I_x^2 \rangle^{1/2}$  and  $\langle I_y^2 \rangle^{1/2}$  for the levels with  $I - j = \text{even}$ , while open circles connected by dashed lines show the corresponding results for  $I - j = \text{odd}$ . The closed triangles connected by solid lines show  $\langle j_x^2 \rangle^{1/2}$  and  $\langle j_y^2 \rangle^{1/2}$  for the levels with  $I - j = \text{even}$ , while the open triangles connected by dashed lines show the corresponding results for  $I - j = \text{odd}$ . The parameters are  $\mathcal{J}_0 = 25 \text{ MeV}^{-1}$ ,  $V = 1.6 \text{ MeV}$ ,  $\beta_2 = 0.18$ , and  $\gamma = 26^\circ$ .



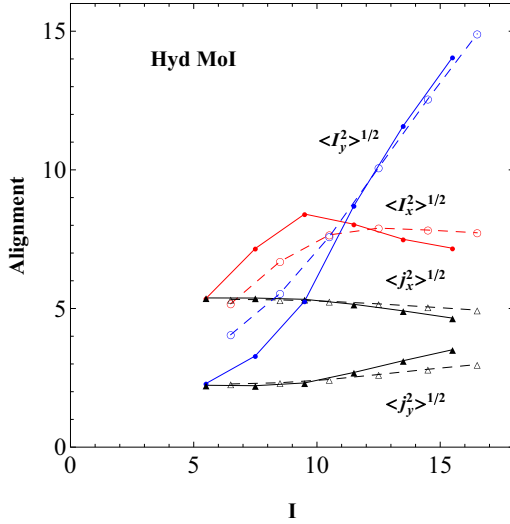


FIG. 10. The alignments of  $\langle I_x^2 \rangle^{1/2}$ ,  $\langle I_y^2 \rangle^{1/2}$ ,  $\langle j_x^2 \rangle^{1/2}$ , and  $\langle j_y^2 \rangle^{1/2}$  for the hydrodynamical (hyd) Mol as functions of  $I$ . The solid circles connected by solid lines show  $\langle I_x^2 \rangle^{1/2}$  and  $\langle I_y^2 \rangle^{1/2}$  for the levels with  $I - j = \text{even}$ , while the open circles connected by dashed lines show the corresponding results for  $I - j = \text{odd}$ . The closed triangles connected by solid lines show  $\langle j_x^2 \rangle^{1/2}$  and  $\langle j_y^2 \rangle^{1/2}$  for the levels with  $I - j = \text{even}$ , while the open triangles connected by dashed lines show the corresponding results for  $I - j = \text{odd}$ . The parameter set is the same as in Fig. 9.

$\langle I_x^2 \rangle^{1/2}$  is the largest at the beginning of the band and then  $\langle I_y^2 \rangle^{1/2}$  increases rapidly and becomes the largest. Although  $\langle j_x^2 \rangle^{1/2}$  and  $\langle j_y^2 \rangle^{1/2}$  keep constant for the small  $I$ , they start to oscillate between  $I - j = \text{even}$  and odd lines with increasing  $I$ . The difference in  $\langle I_x^2 \rangle^{1/2}$  or  $\langle I_y^2 \rangle^{1/2}$  between the solid and dashed lines never becomes one unit.

### B. Diagonal boson representation for $I_y$ and $j_x$ (transverse case)

Keeping in mind the behavior of the alignments shown in Fig 10, we employ the diagonal representation both for  $I_y$  and  $j_x$ :

$$\begin{aligned} I_+ &= I_-^\dagger = I_z + iI_x = -\hat{a}'^\dagger \sqrt{2I - \hat{n}_{a'}}, \\ I_y &= I - \hat{n}_{a'}, \quad \text{with} \quad \hat{n}_{a'} = \hat{a}'^\dagger \hat{a}'; \\ j_+ &= j_-^\dagger = j_y + ij_z = \sqrt{2j - \hat{n}_{b'}} \hat{b}', \\ j_x &= j - \hat{n}_{b'}, \quad \text{with} \quad \hat{n}_{b'} = \hat{b}'^\dagger \hat{b}'. \end{aligned} \quad (44)$$

We diagonalize  $H_{\text{rot}} + H_{\text{sp}}$  in the next-to-leading order expansion in the boson-number operators  $\hat{n}_{a'}$  and  $\hat{n}_{b'}$ . To eliminate the linear terms  $i\sqrt{2I}jA_x^{\text{hyd}}(\hat{a}' - \hat{a}'^\dagger)$  and  $i\sqrt{2j}IA_y^{\text{hyd}}(\hat{b}'^\dagger + \hat{b}')$ , we apply the unitary transformation giving constant shifts to the boson operators:

$$\hat{a}' = \hat{a} + p, \quad \hat{b}' = \hat{b} + q. \quad (45)$$

Then,  $p$  becomes purely imaginary, so we put  $p = ir$  and obtain

$$r = \sqrt{\frac{I}{2}} \frac{jA_x^{\text{hyd}}}{A - B}, \quad q = \sqrt{\frac{j}{2}} \frac{IA_y^{\text{hyd}}}{C + D}, \quad (46)$$

where  $A$ ,  $B$ ,  $C$ , and  $D$  are defined by

$$\begin{aligned} A &= \frac{I}{2}(A_z^{\text{hyd}} + A_x^{\text{hyd}} - 2A_y^{\text{hyd}})\left(1 - \frac{1}{2I}\right), \\ B &= \frac{I}{2}(A_z^{\text{hyd}} - A_x^{\text{hyd}})\left(1 - \frac{1}{4I}\right), \\ C &= \frac{j}{2}\left[A_y^{\text{hyd}} + A_z^{\text{hyd}} - 2A_x^{\text{hyd}} + \frac{6V}{j(j+1)}\cos\left(\gamma - \frac{\pi}{3}\right)\right] \\ &\quad \times \left(1 - \frac{1}{2j}\right), \\ D &= \frac{j}{2}\left[A_y^{\text{hyd}} - A_z^{\text{hyd}} + \frac{2\sqrt{3}V}{j(j+1)}\sin\left(\gamma - \frac{\pi}{3}\right)\right]\left(1 - \frac{1}{4j}\right). \end{aligned} \quad (47)$$

We arrive at an approximate Hamiltonian written in terms of two kinds of HP bosons ( $\hat{a}, \hat{a}^\dagger, \hat{b}, \hat{b}^\dagger$ ), i.e.,  $H_B \cong H_0 + H_2 + H_3 + H_4$ , where  $H_0$  denotes a constant which collects all the terms independent of boson operators,  $H_2$  the bilinear forms of boson operators, and the residual  $H_3$  and  $H_4$  third and fourth order forms, respectively. With Eqs. (46) and (47),  $H_0$  becomes

$$\begin{aligned} H_0 &= A_x^{\text{hyd}}j(j+1) + A_y^{\text{hyd}}I(I+1) - 2V\cos\left(\gamma - \frac{\pi}{3}\right) \\ &\quad - \frac{I(jA_x^{\text{hyd}})^2}{A - B} - \frac{j(IA_y^{\text{hyd}})^2}{C + D} - \frac{1}{4}(A_x^{\text{hyd}} + A_y^{\text{hyd}} - 2A_z^{\text{hyd}}) \\ &\quad + \frac{3V}{2j(j+1)}\cos\left(\gamma - \frac{\pi}{3}\right). \end{aligned} \quad (48)$$

The  $H_2$  term is expressed in the form

$$H_2 = \begin{pmatrix} \hat{a} & \hat{b} & \hat{a}^\dagger & \hat{b}^\dagger \end{pmatrix} \begin{pmatrix} A & iF & B & -iF \\ -iF & C & -iF & D \\ B & iF & A & -iF \\ iF & D & iF & C \end{pmatrix} \begin{pmatrix} \hat{a}^\dagger \\ \hat{b}^\dagger \\ \hat{a} \\ \hat{b} \end{pmatrix}, \quad (49)$$

where  $F = \sqrt{Ij}/2A_z^{\text{hyd}}$ . In this next-to-leading order approximation, the stability condition is derived from the two positive solutions of  $2\omega_{(\pm)}^2 = b \pm \sqrt{b^2 - 4c}$  with

$$\begin{aligned} b &\equiv A^2 - B^2 + C^2 - D^2, \\ c &\equiv (A^2 - B^2)(C^2 - D^2) - 4F^2(A - B)(C + D). \end{aligned} \quad (50)$$

In Fig. 11, we show the domain where the stability conditions are satisfied. The solid lines are for the levels with  $I = 11/2$  and  $31/2$  ( $I - j = \text{even}$ ), and the dashed lines for  $I = 13/2$  and  $33/2$  ( $I - j = \text{odd}$ ). The stability domains for the other levels are located between these border lines. In the region  $13^\circ \leq \gamma \leq 30^\circ$ , this model gives a stability domain for  $V = 1.6 \text{ MeV}$ .

Now we go back to the leading order approximation, in which the factors  $(1 - \frac{1}{2I})$  in  $A$ ,  $(1 - \frac{1}{4I})$  in  $B$ ,  $(1 - \frac{1}{2j})$  in  $C$ , and  $(1 - \frac{1}{4j})$  in  $D$  are replaced by 1 in Eq. (47), and the last two terms in Eq. (48) do not exist. Then, the values of  $b$  and  $c$

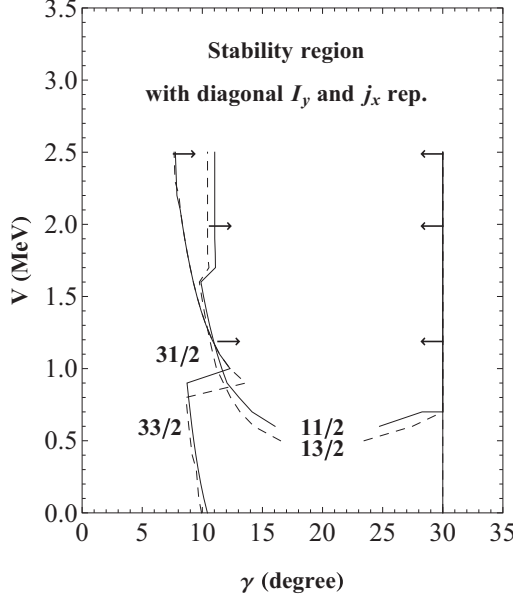


FIG. 11. Stability domain in the  $\gamma$ - $V$  plane for hydrodynamical MoI with diagonal representation of  $I_y$  and  $j_x$  in the next-to-leading order approximation. The solid lines correspond to the yrast levels of  $I = 11/2$  and  $31/2$  ( $I - j = \text{even}$ ), while the dashed lines correspond to those of  $I = 13/2$  and  $33/2$  ( $I - j = \text{odd}$ ). The domain borders for the other levels are between these lines. The arrows attached to the lines indicate the region where stability conditions are satisfied.

are calculated from these new  $A$ ,  $B$ ,  $C$ , and  $D$  as

$$b = I^2(A_x^{\text{hyd}} - A_y^{\text{hyd}})(A_z^{\text{hyd}} - A_y^{\text{hyd}}) \left[ 1 + V_1 V_2 \left( \frac{j}{I} \right)^2 \right],$$

$$c = [Ij(A_x^{\text{hyd}} - A_y^{\text{hyd}})(A_z^{\text{hyd}} - A_y^{\text{hyd}})]^2$$

$$\times V_1 \left[ V_2 - \left( \frac{A_z^{\text{hyd}}}{A_z^{\text{hyd}} - A_y^{\text{hyd}}} \right)^2 \right], \quad (51)$$

where

$$V_1 = \frac{2\sqrt{3}V \sin \gamma}{j(j+1)(A_x^{\text{hyd}} - A_y^{\text{hyd}})} - 1, \quad (52)$$

$$V_2 = \frac{2\sqrt{3}V \sin(\gamma + \frac{\pi}{3})}{j(j+1)(A_z^{\text{hyd}} - A_y^{\text{hyd}})} + \frac{A_z^{\text{hyd}} - A_x^{\text{hyd}}}{A_z^{\text{hyd}} - A_y^{\text{hyd}}}.$$

Then the squares of the two positive eigenvalues are

$$2\omega_{(\pm)}^2 = I^2(A_x^{\text{hyd}} - A_y^{\text{hyd}})(A_z^{\text{hyd}} - A_y^{\text{hyd}}) \left[ 1 + V_1 V_2 \left( \frac{j}{I} \right)^2 \right]$$

$$\pm \sqrt{\left( 1 - V_1 V_2 \left( \frac{j}{I} \right)^2 \right)^2 + V_1 \left( \frac{2jA_z^{\text{hyd}}}{I(A_z^{\text{hyd}} - A_y^{\text{hyd}})} \right)^2}. \quad (53)$$

In the asymptotic region of  $j/I \ll 1$ , we get  $\omega_{(+)}^2 \simeq I^2(A_x^{\text{hyd}} - A_y^{\text{hyd}})(A_z^{\text{hyd}} - A_y^{\text{hyd}})$ , which is nothing but the ex-

citation energy of the wobbling mode around the  $y$  axis with the maximum MoI  $\mathcal{J}_y^{\text{hyd}}$ , as was proposed by Bohr and Mottelson [1]. For the other energy  $\omega_{(-)}^2$ , we get

$$\omega_{(-)}^2 \simeq j^2(A_x^{\text{hyd}} - A_y^{\text{hyd}})(A_z^{\text{hyd}} - A_y^{\text{hyd}})$$

$$\times V_1 \left[ V_2 - \left( \frac{A_z^{\text{hyd}}}{A_z^{\text{hyd}} - A_y^{\text{hyd}}} \right)^2 \right]. \quad (54)$$

This expression indicates that the excitation energy  $\omega_{(-)}$  is associated with the precession mode of  $\vec{j}$  because it vanishes for  $j = 0$ . If we continue further the calculation of the alignments  $\langle I_y^2 \rangle^{1/2}$  and  $\langle j_y^2 \rangle^{1/2}$  for larger  $I \geq 33/2$  in Fig. 10, they show a similar behavior as in Fig. 6, indicating that  $\omega_{(-)}^2$  is the  $j$ -precession mode around the axis with the maximum MoI. The potential effect becomes negligible compared with the Coriolis term for larger  $I$ .

Now we consider the case of  $I = j$  in Eq. (53). The expression under the square root in Eq. (53) is well approximated by

$$\left[ 1 + V_1 \left( V_2 - \frac{1}{2} \left( \frac{A_z}{A_z - A_y} \right)^2 \right) \right]^2, \quad (55)$$

because the remaining part is only 1%. In this case, we get

$$4\omega_{(-)}^2 \sim \frac{I^2 A_z^2}{A_z - A_y} \left( \frac{\sqrt{3}V}{j(j+1)} + A_y - A_x \right). \quad (56)$$

This approximate expression still gives the domain border, but it indicates neither the wobbling mode nor the precession mode.

To clarify the physical contents of elementary excitations with  $\omega_{(\pm)}$ , we solve the eigenvalue equation using the wave functions defined in Eq. (25) for  $H_2$  given in Eq. (49) together with the orthonormality relations of Eq. (27). In this framework,  $\omega_{(+)}$  corresponds to  $\omega_\alpha$ , and  $\omega_{(-)}$  to  $\omega_\beta$ . Using the eigenvalues  $\omega_{(\pm)}$ , we express all the components of the eigenvectors as

$$u_\pm = (A - B \pm \omega_{(+)})[(C + D)(2F^2 - BC + BD)$$

$$+ B\omega_{(+)}^2]N_+,$$

$$v_\pm = \pm iF(C + D \pm \omega_{(+)})[(A - B)^2 - \omega_{(+)}^2]N_+,$$

$$w_\pm = (A - B \pm \omega_{(-)})[(C + D)(2F^2 - BC + BD)$$

$$+ B\omega_{(-)}^2]N_-,$$

$$t_\pm = \pm iF(C + D \pm \omega_{(-)})[(A - B)^2 - \omega_{(-)}^2]N_-, \quad (57)$$

where the normalization constants are defined by

$$N_\pm^{-2} = 4\omega_{(\pm)}[(A - B)[(C + D)(2F^2 - BC + BD) + B\omega_{(\pm)}^2]$$

$$+ F^2(C + D)((A - B)^2 - \omega_{(\pm)}^2)^2]. \quad (58)$$

In Fig. 12, we show the evolution of squared amplitudes  $|u_\pm|^2$  (solid circles),  $|v_\pm|^2$  (solid triangles),  $|w_\pm|^2$  (open circles), and  $|t_\pm|^2$  (open triangles) with increasing  $I$ . Because of the small values of  $|w_-|^2$  and  $|t_-|^2$ , they are not clearly discriminated in the figure. These eight amplitudes satisfy the orthonormality relations of Eq. (27). Note that there

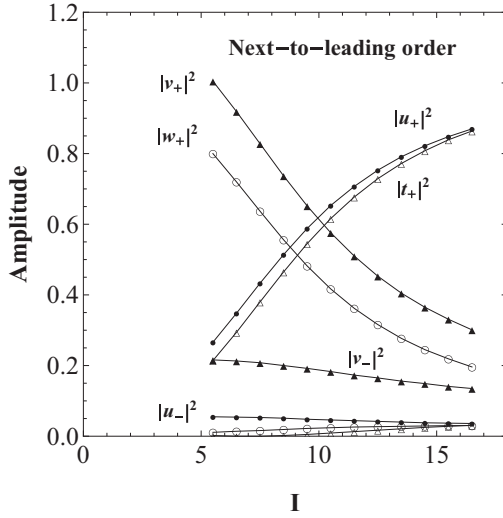


FIG. 12. Comparison of the squared absolute amplitudes in Eq. (27) in the next-to-leading order approximation as functions of  $I$ . The solid circles correspond to  $|u_+|^2$ , solid triangles to  $|v_+|^2$ , open circles to  $|w_+|^2$ , and open triangles to  $|t_+|^2$ . Both  $|w_-|^2$  and  $|t_-|^2$  are quite small and lie along the abscissa. The parameter set is the same as in Fig. 9.

occurs the crossover between the decreasing amplitude ( $|v_+|^2$  and  $|w_+|^2$ ) and the increasing ones ( $|u_+|^2$  and  $|t_+|^2$ ) around  $I = 17/2 \sim 21/2$ . By the inverse transformation of Eq. (25), the quasiboson operators  $\alpha$  and  $\beta$  are expressed in terms of the boson operators  $\hat{a}$  and  $\hat{b}$ :

$$\begin{aligned}\alpha^\dagger &= u_+ \hat{a}^\dagger - u_- \hat{a} + v_+ \hat{b}^\dagger - v_- \hat{b}, \\ \beta^\dagger &= w_+ \hat{a}^\dagger - w_- \hat{a} + t_+ \hat{b}^\dagger - t_- \hat{b}.\end{aligned}\quad (59)$$

Comparing Eq. (59) with the results in Fig. 12, we find that  $\hat{b}$  dominates as the main component of  $\alpha$ , and  $\hat{a}$  as that of  $\beta$ , for low  $I$  ( $\leq 13/2$ ). However, for high  $I$  ( $\geq 29/2$ ),  $\hat{b}$  dominates as the main component of  $\beta$ , and  $\hat{a}$  as that of  $\alpha$ . The eigenvector corresponding to  $\omega_{(-)}$  is given by  $(w_+, t_+, w_-, t_-)$ , while the one corresponding to  $\omega_{(+)}$  is given by  $(u_+, v_+, u_-, v_-)$ . In other words, for low  $I$  the lower mode with  $\omega_{(-)}$  ( $n_\beta = 1$ ) is related to  $\vec{I}$ , and the higher mode with  $\omega_{(+)}$  ( $n_\alpha = 1$ ) is related to  $\vec{j}$ . For high  $I$ , the lower mode with  $\omega_{(-)}$  ( $n_\beta = 1$ ) corresponds to  $\vec{j}$ , and the higher mode with  $\omega_{(+)}$  ( $n_\alpha = 1$ ) to  $\vec{I}$ , which agrees with the prediction based on the expression in Eq. (54).

The original bosons to describe the particle-rotor model with hydrodynamical MoI are not  $\hat{a}$  and  $\hat{b}$  but  $\hat{a}'$  and  $\hat{b}'$ , which are related to  $\hat{a}$  and  $\hat{b}$  through Eq. (45). These shift transformations were determined to eliminate linear terms in the boson operators  $\hat{a}$ ,  $\hat{a}^\dagger$ ,  $\hat{b}$ , and  $\hat{b}^\dagger$ . In Fig. 13, we show the behavior of  $r^2$  (solid circle) and  $q^2$  (open circles) defined in Eq. (46) calculated in the next-to-leading order approximation. According to the decrease of  $r^2$  and the increase of  $q^2$  with increasing  $I$ , the physical quantities evolve with  $I$ . Figure 13 shows that  $r^2$  becomes large for low  $I$ , while  $q^2$  becomes large for high  $I$ . As seen in Fig. 12 in the low spin region of  $I \sim j$ , the amplitudes of  $|v_+|^2$  and  $|w_+|^2$  are dominant ( $\sim 1$ ), while

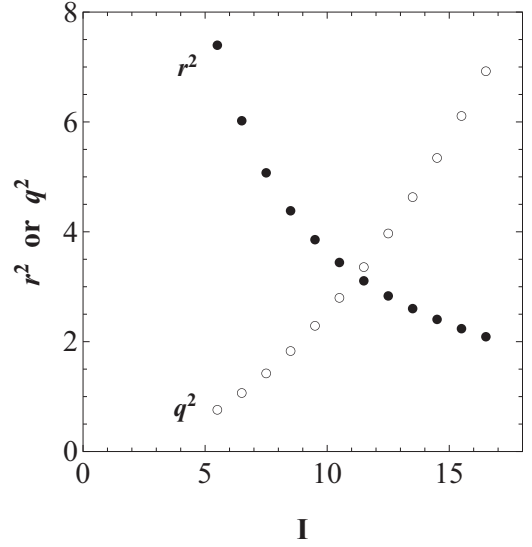


FIG. 13. The square of shift parameters  $r^2$  and  $q^2$  as functions of  $I$  in the next-to-leading order approximation. The solid circles correspond to  $r^2$ , and open circles to  $q^2$ . The parameter set is the same as in Fig. 9.

the rest is small. However, in the high spin region of  $I \gg j$ ,  $|u_+|^2$  and  $|t_+|^2$  are dominant ( $\sim 1$ ), while the rest is small.

To discuss the physical contents in both asymptotic regions, keeping only these dominant amplitudes  $|u_+|^2$ ,  $|v_+|^2$ ,  $|w_+|^2$ , and  $|t_+|^2$  relevant to the harmonic excitation described by  $\omega_{(-)}(2\hat{n}_\beta + 1)$ , we express  $I_x^2$ ,  $I_y^2$ ,  $j_x^2$ , and  $j_y^2$  as

$$\begin{aligned}I_x^2 &\sim r^2 \left( 2I - r^2 - \frac{3}{4} \right) + \frac{I}{2} \\ &\quad + \hat{n}_\beta |w_+|^2 \left( I - \frac{1}{2} - \frac{7}{2} r^2 + \frac{|w_+|^2}{2} \right),\end{aligned}\quad (60a)$$

$$\begin{aligned}I_y^2 &\sim (I - r^2)^2 + r^2 (|u_+|^2 + |w_+|^2) \\ &\quad + \hat{n}_\beta |w_+|^2 \{ 2(2r^2 - I) + |u_+|^2 \},\end{aligned}\quad (60b)$$

and

$$\begin{aligned}j_x^2 &\sim (j - q^2)^2 + q^2 (|v_+|^2 + |t_+|^2) \\ &\quad + \hat{n}_\beta |t_+|^2 \{ 2(2q^2 - j) + |v_+|^2 \},\end{aligned}\quad (61a)$$

$$\begin{aligned}j_y^2 &\sim q^2 \left( 2j - q^2 - \frac{3}{4} \right) + \frac{j}{2} \\ &\quad + \hat{n}_\beta |t_+|^2 \left( j - \frac{1}{2} - \frac{7}{2} q^2 + \frac{|t_+|^2}{2} \right).\end{aligned}\quad (61b)$$

In the region of  $I \sim j$ , due to the large value of  $r^2$ , the coefficient of  $\hat{n}_\beta$  in Eq. (60a) becomes negative, while the one in Eq. (60b) becomes positive. As a consequence, the dashed line for  $\langle I_x^2 \rangle^{1/2}$  in Fig. 10 is located lower than the solid line, and the dashed line for  $\langle I_y^2 \rangle^{1/2}$  higher than the solid line. In contrast, in the region of  $I \gg j$  ( $I \geq 29/2$ ), due to the small value of  $r^2$ , the coefficient of  $\hat{n}_\beta$  in Eq. (60a) becomes positive, while the one in Eq. (60b) becomes negative. As a consequence, the dashed line for  $\langle I_x^2 \rangle^{1/2}$  in Fig. 10 is located higher than

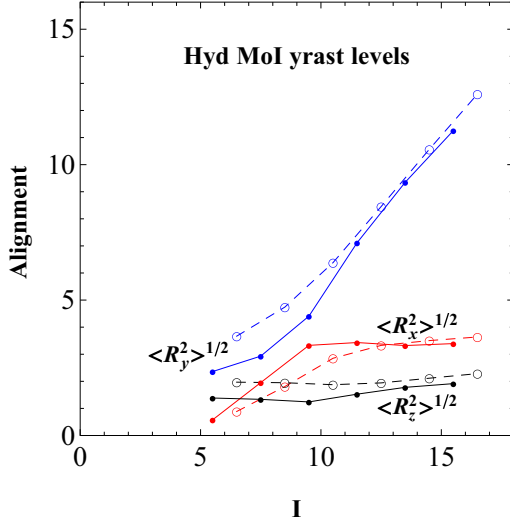


FIG. 14. The alignments of  $\langle R_x^2 \rangle^{1/2}$ ,  $\langle R_y^2 \rangle^{1/2}$ , and  $\langle R_z^2 \rangle^{1/2}$  for the hydrodynamical (hyd) MoI as functions of  $I$ . The solid lines are for the levels with  $I - j = \text{even}$ , while the dashed lines for those with  $I - j = \text{odd}$ . The parameter set is the same as in Fig. 9.

the solid line, and the dashed line for  $\langle I_y^2 \rangle^{1/2}$  lower than the solid line. The difference between the solid and dashed lines becomes smaller due to the decrease of  $|w_+|^2$ . As for  $\langle I_y^2 \rangle^{1/2}$ , the large value of  $|u_+|^2$  works to decrease the difference.

Similarly, in the region of  $I \sim j$ , due to the small value of  $q^2$ , the coefficient of  $\hat{n}_\beta$  in Eq. (61a) becomes negative, while the one in Eq. (61b) becomes positive. As a consequence, the dashed line for  $\langle j_x^2 \rangle^{1/2}$  in Fig. 10 is located lower than the solid line, and the dashed line for  $\langle j_y^2 \rangle^{1/2}$  higher than the solid line, although the difference is small due to the small value of  $|t_+|^2$ . In contrast, in the region of  $I \gg j$  ( $I \geq 29/2$ ), due to the large value of  $q^2$ , the coefficient of  $\hat{n}_\beta$  in Eq. (61a) becomes positive, while the one in Eq. (61b) becomes negative. As a consequence, the dashed line for  $\langle j_x^2 \rangle^{1/2}$  in Fig. 10 is located higher than the solid line, and the dashed line for  $\langle j_y^2 \rangle^{1/2}$  lower than the solid line.

We expect that the behavior of the core angular momentum  $\vec{R} = \vec{I} - \vec{j}$  gives direct information about the wobbling motion of the triaxially deformed core. In Fig. 14, we plot the exact root-mean-square values of  $\langle R_x^2 \rangle^{1/2}$ ,  $\langle R_y^2 \rangle^{1/2}$ , and  $\langle R_z^2 \rangle^{1/2}$ . First of all,  $\langle R_y^2 \rangle^{1/2}$  is the largest through the whole region from  $I = 11/2$  to  $33/2$ , so that the body rotates around the  $y$  axis with the maximum MoI. Moreover, there is no staggering to indicate a wobbling mode in  $\langle R_y^2 \rangle^{1/2}$ , because  $I - j = \text{even}$  (solid line) runs below  $I - j = \text{odd}$  (dashed line) and the difference is not unity. For comparison, we show the rigid MoI case in Fig. 15, which demonstrates typical behavior of the alignment of  $\vec{R}$  when the wobbling mode occurs around the  $x$  axis with maximum MoI. Note that the increment of the alignment  $\langle R_x^2 \rangle^{1/2}$  is well quantized by one unit, which is similar to the case of  $\langle I_x^2 \rangle^{1/2}$  in Fig. 9. As a typical characteristic of the wobbling mode around the  $x$  axis with the largest MoI, the following identities hold:

$$\langle R_x^2 \rangle_I^{1/2} \simeq \langle R_x^2 \rangle_{I+1}^{1/2} \text{ for } I - j = \text{even}, \quad (62a)$$

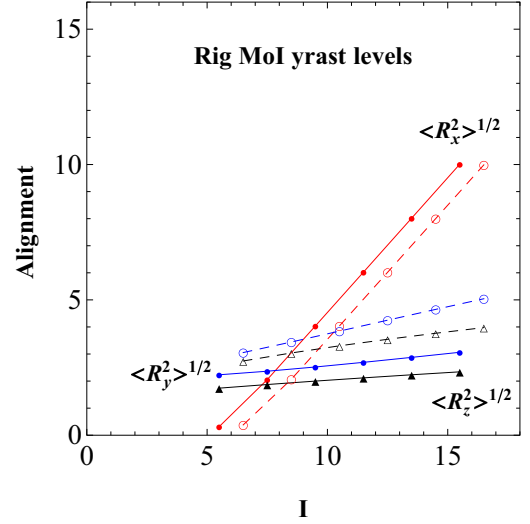


FIG. 15. The alignments of  $\langle R_x^2 \rangle^{1/2}$ ,  $\langle R_y^2 \rangle^{1/2}$ , and  $\langle R_z^2 \rangle^{1/2}$  for the rigid (rig) MoI as functions of  $I$ . The solid and open circles correspond to  $\langle R_x^2 \rangle^{1/2}$  and  $\langle R_y^2 \rangle^{1/2}$ , while solid and open triangles correspond to  $\langle R_z^2 \rangle^{1/2}$ . The solid lines are for the levels with  $I - j = \text{even}$ , while the dashed lines for those with  $I - j = \text{odd}$ . The parameter set is the same as in Fig. 9.

and

$$\langle R_x^2 \rangle_{I+2}^{1/2} - \langle R_x^2 \rangle_I^{1/2} \simeq 2. \quad (62b)$$

The behavior of the three angular momenta  $\vec{I}$ ,  $\vec{j}$ , and  $\vec{R} \equiv \vec{I} - \vec{j}$  are illustrated in Fig. 16(a) for the lowest spin state with  $I = j = 11/2$ , and in Fig. 16(b) for a higher spin state with  $I = 31/2$ . The quantization axis is assigned to the  $x$  axis in Fig. 16(a) and to the  $y$  axis in Fig. 16(b). The domains where the heads of angular-momentum vectors move are symbolized by closed loops, being depicted in a way consistent with the exact results of the root-mean-square values  $\langle I_k^2 \rangle^{1/2}$ ,  $\langle j_k^2 \rangle^{1/2}$ , and  $\langle R_k^2 \rangle^{1/2}$  ( $k = x, y, z$ ). The vector heads of  $\vec{I}$  and  $\vec{j}$  are on the spheres with definite radii  $\sqrt{I(I+1)}$  and  $\sqrt{j(j+1)}$ , respectively. The loop for  $\vec{I}$  in the figure represents the intersection between the sphere and an elliptic cylinder, whose projection onto the  $zx$  plane is an ellipse with semimajor axis  $\langle I_x^2 \rangle^{1/2}$  and semiminor axis  $\langle I_z^2 \rangle^{1/2}$  for the case  $I = 31/2$  as shown in Fig. 16(b). The way to draw the loop for  $\vec{j}$  is the same as that for  $\vec{I}$  in Fig. 16(b). However, the two loops for  $\vec{I}$  and  $\vec{j}$  in Fig. 16(a) are located very close to each other because of the equality  $I = j$  and the fact that the exact result gives  $\langle I_y^2 \rangle^{1/2} \sim \langle j_y^2 \rangle^{1/2} \sim 2.2$  and  $\langle I_z^2 \rangle^{1/2} \sim \langle j_z^2 \rangle^{1/2} \sim 1.3$ . These values are the same as those displayed in Figs. 10 and 14.

As for the vector  $\vec{R}$  whose square does not commute with the Hamiltonian, we depict the corresponding loop as an intersection between the sphere with its radius  $\langle R_x^2 + R_y^2 + R_z^2 \rangle^{1/2}$  and an elliptic cylinder with the semimajor axis  $\langle R_y^2 \rangle^{1/2}$  and the semiminor axis  $\langle R_z^2 \rangle^{1/2}$  for Fig. 16(a), and with the semimajor axis  $\langle R_x^2 \rangle^{1/2}$  and the semiminor axis  $\langle R_z^2 \rangle^{1/2}$  for Fig. 16(b). In Fig. 16(a)  $\vec{I}$ ,  $\vec{j}$ , and  $\vec{R}$  compose an isosceles triangle with

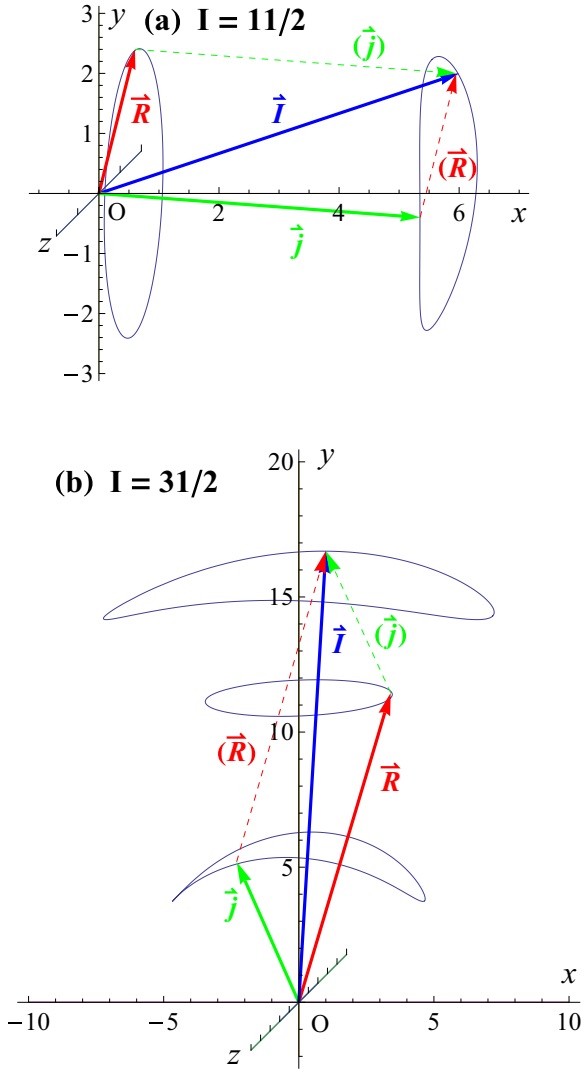


FIG. 16. Behavior of three angular momenta  $\vec{I}$ ,  $\vec{j}$ , and  $\vec{R}(\equiv \vec{I} - \vec{j})$  for the hydrodynamical MoI. (a) The case of the lowest spin state of  $I = j = 11/2$ , and (b) the one of the high spin state of  $I = 31/2$ . Both drawings are designed in consistence with the exact results of the root mean squares of angular-momentum components. Further details are presented in the text.

sides of  $I (=j)$ . We observe that the vector  $\vec{R}$  describing the rotation of the triaxial body moves very close to the  $y$  axis with the largest MoI already from  $I = j (= 11/2)$ , and keeps a similar behavior also for higher spin states. Comparing the sizes of loops, we recognize that the extent of the precession

of  $\vec{R}$  about the  $y$  axis is narrower than that of  $\vec{I}$ . Note that  $\vec{R}$  is nearly perpendicular to the  $x$  axis with medium MoI through the whole range of  $I$ .

#### IV. REPRODUCTION OF EXPERIMENTAL DATA USING RIGID MOI

In reproducing the electromagnetic transition rates, we are faced with a defect when using the hydrodynamical MoI. We compare  $B(E2)_{\text{out}}/B(E2)_{\text{in}}$  calculated with hydrodynamical and rigid MoI in Table I, and  $B(M1)_{\text{out}}/B(E2)_{\text{in}}$  in Table II as functions of  $\gamma$  and  $I$  of the initial state. The other parameters are the same as those used in Fig. 9. As seen in Table I, the use of the hydrodynamical MoI gives smaller  $B(E2)_{\text{out}}/B(E2)_{\text{in}}$  values than the use of the rigid MoI. Because  $B(E2)_{\text{out}}/B(E2)_{\text{in}}$  is proportional to  $\tan^2 \gamma$ , both types of MoI give increasing values with increasing  $\gamma$ . The decrease of the ratio  $B(E2)_{\text{out}}/B(E2)_{\text{in}}$  with increasing  $I$  is more rapid for hydrodynamical MoI than the one for rigid MoI. In Table II, the ratio  $B(M1)_{\text{out}}/B(E2)_{\text{in}}$  is proportional to  $(g_{\text{eff}}/Q_0)^2$ , where we adopt  $g_{\text{eff}} = 0.414$ , which is obtained from the bare value of  $g_{\ell} - g_R + (g_s - g_{\ell})/(2j)$  multiplied by the quenching factor 0.5. The value of  $Q_0$  is estimated from the following formula with the radius given by Eq. (7):

$$Q_0 = \frac{Z}{5} (2r_z^2 - r_x^2 - r_y^2) = \frac{3}{\sqrt{5}\pi} Z R_0^2 \beta_2 \cos \gamma, \quad (63)$$

which gives  $Q_0 = 3 \cos \gamma$  b for  $^{135}\text{Pr}$  with  $\beta_2 = 0.18$ . In contrast to the case of  $B(E2)_{\text{out}}/B(E2)_{\text{in}}$ , the use of hydrodynamical MoI gives larger values of  $B(M1)_{\text{out}}/B(E2)_{\text{in}}$  than using rigid MoI, and decreases slowly at high spin. The large value of  $B(M1)_{\text{out}}/B(E2)_{\text{in}}$  at high spin excludes the possibility of hydrodynamical MoI for the wobbling mode in Lu isotopes [14] unless the sign of  $\gamma$  is changed [22].

There is no way to take into account the pairing effect microscopically when using hydrodynamical MoI. However, the pairing effect on the MoI is well taken into account by using the rigid MoI [1,18,23]. The integrand after the closure approximation to the cranking formula is carefully approximated and the analytical formula was obtained in Ref. [18], which agrees quite well with the results obtained in Refs. [1,23]. This approximation method is extended to the gap equation, which takes into account the Coriolis antipairing (CAP) effect and the blocking effect. The other approximation methods of Refs. [1,23] are not applicable to this gap equation.

TABLE I. Comparison of  $B(E2)_{\text{out}}/B(E2)_{\text{in}}$  between hydrodynamical (hyd) and rigid (rig) MoI as functions of  $\gamma$  and  $I$  of the initial state.

Initial $I$	$\gamma = 10^\circ$		$\gamma = 18^\circ$		$\gamma = 26^\circ$	
	Hyd MoI	Rig MoI	Hyd MoI	Rig MoI	Hyd MoI	Rig MoI
21/2	0.0818	0.289	0.227	0.606	0.416	1.161
25/2	0.0628	0.234	0.158	0.496	0.273	0.954
29/2	0.0498	0.197	0.106	0.420	0.181	0.812
33/2	0.0404	0.170	0.071	0.364	0.124	0.707



TABLE II. Comparison of  $B(M1)_{\text{out}}/B(E2)_{\text{in}}$  between hydrodynamical (hyd) MoI and rigid (rig) MoI as functions of  $\gamma$  and  $I$  of the initial state.

Initial $I$	$\gamma = 10^\circ$		$\gamma = 18^\circ$		$\gamma = 26^\circ$	
	Hyd MoI	Rig MoI	Hyd MoI	Rig MoI	Hyd MoI	Rig MoI
21/2	0.213	0.174	0.294	0.324	0.528	0.543
25/2	0.165	0.120	0.273	0.228	0.681	0.386
29/2	0.134	0.088	0.276	0.168	0.656	0.289
33/2	0.112	0.067	0.257	0.129	0.563	0.223

For highly excited states the angular-momentum dependence through the decreasing pairing gap caused by the CAP effect is well simulated by a two parameter fitting of the rigid MoI [10–12]. However, these two parameters are determined at very high spin and highly excited states, where the average pairing gap is small. In the  $^{135}\text{Pr}$  case, these levels are before the first backbending caused by the gapless superconductor [24–29]. In such a case we have to refer to the detailed behavior of MoI as a function of  $I$ , which has been derived from the HFB analysis [18].

In reference to the  $I$ -dependent curve as displayed in Fig. 9 in Ref. [18], which is derived by the perturbation treatment of the CAP effect on an odd- $A$  nucleus, we assume a simplified functional form for the  $I$  dependence of the rigid MoI:

$$\frac{\mathcal{J}_0}{1 + \exp(-(I - \bar{b})/\bar{a})}. \quad (64)$$

We choose the two parameters as  $\bar{a} = 7.5$  and  $\bar{b} = 15.5$ . The other parameters are  $\beta_2 = 0.18$ ,  $V = 1.6$  MeV,  $\mathcal{J}_0 = 25 \text{ MeV}^{-1}$ , and  $\gamma = 18^\circ$ , which are the same as in Fig. 9 except for  $\gamma$ .

In Fig. 17, we compare the calculated energy level relative to the reference  $E(I) - 0.02I(I + 1)$  as functions of the angular momentum  $I$ , together with the experimental ones [13,19]. The theoretical values are normalized at  $I = 11/2$  in band

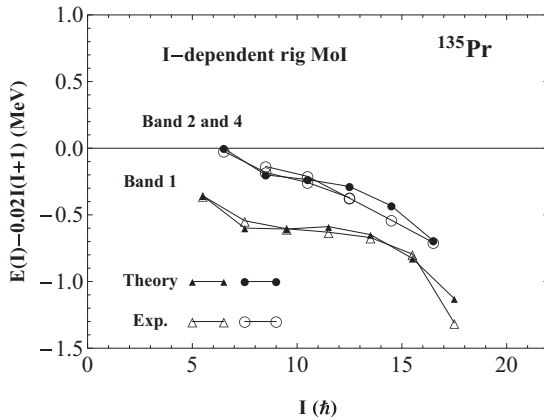


FIG. 17. Comparison of  $E(I) - 0.02I(I + 1)$  between theoretical results and experimental data in Refs. [13,19]. Theoretical values are shown by solid triangles for band 1 and solid circles for bands 2 and 4, while experimental data for band 1 are shown by open triangles and bands 2 and 4 by open circles. Band 2 is from  $I = 13/2$  to  $25/2$ , while band 4 is from  $I = 17/2$  to  $33/2$ .

1. The energies of  $E(I) - 0.02I(I + 1)$  are not sensitive to  $\gamma$ , but  $\gamma = 18^\circ$  seems to be favorable in reproducing the electromagnetic transitions. In Table III, we compare the calculated electromagnetic transition rates and mixing ratios  $\delta$  with the experimental data [13]. The value of  $Q_0$  and  $g_{\text{eff}}$  are the same as adopted in Tables I and II. The mixing ratio  $\delta$  is proportional to  $Q_0/g_{\text{eff}}$ . The theory reproduces all the data quite well over the whole range of  $I$ .

In Fig. 18, we show the plot of  $I$  versus  $\hbar\omega = E_\gamma/2$  for bands 1, 2, and 4 in comparison with the experimental data. The value of  $\hbar\omega$  for the  $I = 13/2$  state is defined by the transition energy  $E_\gamma$  to the  $I = 11/2$  state. The agreement with the experimental data is quite good. As for the difference between band 2 (from  $I = 13/2$  to  $25/2$ ) and band 4 (from  $I = 17/2$  to  $33/2$ ), it may come from the breaking of Bohr's symmetry ( $D_2$  invariance), which is discussed toward the end of Sec. II B.

Then it becomes desirable to reproduce the backbending curve for band 1 through the whole region before and after the first backbending. After the backbending the yrast levels transfer to the new bands where a high- $j$  pair in the neutron shell or in the proton shell is decoupled, i.e., a gapless superconductor [27–29]. We choose a larger  $\mathcal{J}_0 (= 35 \text{ MeV}^{-1})$  for this new decoupled band. The other parameters are kept the same. In Fig. 19, the backbending curve for band 1 is shown. The theoretical decoupled new band is shifted to coincide with

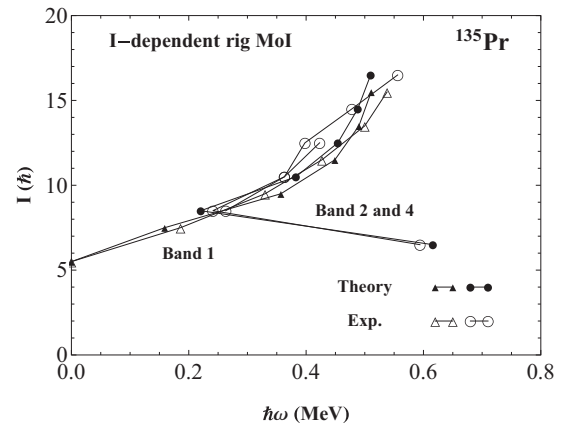


FIG. 18. Comparison between theory and experimental data in the backbending plot for bands 1, 2, and 4. Theoretical values are shown by solid triangles for band 1 and by solid circles for bands 2 and 4, and experimental values are shown by open triangles for band 1, and by open circles for bands 2 and 4.

TABLE III. Comparison of  $B(E2)_{\text{out}}/B(E2)_{\text{in}}$ ,  $B(M1)_{\text{out}}/B(E2)_{\text{in}}$ , and the mixing ratio  $\delta$  between experiment and theory.

$I$	$B(E2)_{\text{out}}/B(E2)_{\text{in}}$		$B(M1)_{\text{out}}/B(E2)_{\text{in}}$		$\delta$	
	Expt.	Theory	Expt.	Theory	Expt.	Theory
17/2		0.648		0.192	$-1.24 \pm 0.13$	-1.13
21/2	$0.843 \pm 0.032$	0.542	$0.164 \pm 0.014$	0.130	$-1.54 \pm 0.09$	-1.34
25/2	$0.500 \pm 0.025$	0.463	$0.035 \pm 0.009$	0.0987	$-2.38 \pm 0.37$	-1.44
29/2	$\geq 0.261 \pm 0.014$	0.402	$\leq 0.016 \pm 0.004$	0.0791		-1.49

the experimental band at  $I = 35/2$ . The agreement is quite good, indicating that the CAP effect is well simulated using two common parameters. Our calculation gives the alignments of  $\vec{I}$ ,  $\vec{j}$ , and  $\vec{R}(=\vec{I}-\vec{j})$  quite similar to those shown in Figs. 9 and 15 whose rigid MoI do not include any  $I$  dependence. Of course, the identities in Eqs. (62a) and (62b) are also satisfied in this calculation with  $I$ -dependent rigid MoI.

## V. CONCLUSION

We have confirmed that two quantum numbers ( $n_\alpha, n_\beta$ ) assigned to each energy level characterize the wobbling mode of the rotor angular momentum  $\vec{R}$  and the precession mode of  $\vec{j}$ . When  $V = 0$ , the lowest level for  $I - j = \text{odd}$  has always (0,1) for hydrodynamical MoI indicating the precession of  $\vec{j}$ . Such a system is well described by choosing a diagonal HP boson representation for both  $I_y$  and  $j_y$ . On the other hand, the lowest level for  $I - j = \text{odd}$  has (1,0) for rigid MoI, indicating the wobbling mode around the axis with maximum MoI. In this case a diagonal HP boson representation is chosen for both  $I_x$  and  $j_x$ . As for the level with  $I = 13/2$ , the lowest level has (0,1) because of the  $D_2$  invariance which prohibits  $R = 1$ . When  $\gamma \sim 0$ , another representation is favorable where  $I_z$  and  $j_z$  are in the diagonal forms. In this case, the two quantum numbers are reduced to  $R = I - j + n_\beta$  and  $R_z = R - n_\alpha$ . The lowest levels are always  $R_z = 0$  or  $n_\alpha = R$

for hydrodynamical MoI. On the contrary, the lowest levels for  $I - j = \text{even}$  have  $R_z = 0$ , but those for  $I - j = \text{odd}$  have  $R_z = 2$  or  $n_\alpha = R - 2$  except for  $I = 13/2$ . This  $R_z = 2$  level splits into  $(r_x, r_y, r_z) = (+1, +1, +1)$  and  $(+1, -1, -1)$  only if Bohr's symmetry is violated and only if the  $D_2$  symmetry is satisfied.

Applying alternative HP boson representations as useful theoretical tools, we have carefully checked the stability equation for the case of hydrodynamical MoI with  $V \neq 0$ . We solved three cases: First, both  $I_x$  and  $j_x$  are represented in the diagonal forms, where we cannot find any stability domain for a fixed  $\gamma$  and  $V$  for  $I > 15/2$ . Second, both  $I_y$  and  $j_y$  are in the diagonal forms, where no stability domain is found for  $V \geq 0.3$  MeV. Third,  $I_y$  and  $j_x$  are in the diagonal forms. In this case the stability domain is found within the region  $13^\circ \leq \gamma \leq 30^\circ$ . The lower harmonic excitation with  $\omega_{(-)}$  for  $I \sim j$  corresponds to the incremental alignment of  $\vec{I}$  along the  $y$  axis with the maximum MoI, while the one for  $I \gg j$  corresponds to the precession of  $\vec{j}$  around the  $y$  axis. In contrast, the mode with  $\omega_{(+)}$  for  $I \gg j$  corresponds to the wobbling of  $\vec{I}$  around the  $y$  axis with the maximum MoI. This crossover occurs at  $I \sim 21/2$ .

A shortage of hydrodynamical MoI is to give a smaller  $B(E2)_{\text{out}}/B(E2)_{\text{in}}$  and larger  $B(M1)_{\text{out}}/B(E2)_{\text{in}}$  compared with rigid MoI. Furthermore, hydrodynamical MoI has no room to include the Coriolis antipairing effect, which is essential in the low-lying rotational levels like in the case of  $^{135}\text{Pr}$ .

There is no wobbling mode around the axis with medium MoI in the particle-rotor model even with the hydrodynamical MoI, as is well known in the pure rotor. Then, there remains the problem of how to describe the experimental data of the band built on the  $I = 11/2^-$  state in  $^{135}\text{Pr}$ . We use a Woods-Saxon-type expression to simulate the  $I$  dependence of the rigid MoI with two parameters, which is obtained from the perturbation treatment of the CAP effect [18]. The particle-rotor model with  $I$ -dependent rigid MoI gives a typical wobbling band and attains a quite good reproduction of the experimental data not only for the energy of the levels, but also for the electromagnetic transition rates and the mixing ratios  $\delta$ .

## ACKNOWLEDGMENTS

The authors express their sincere thanks to the referee for the valuable comments, which stimulated their deeper thinking of this subject. The authors are grateful to Prof. W. Bentz for his careful reading of this manuscript.

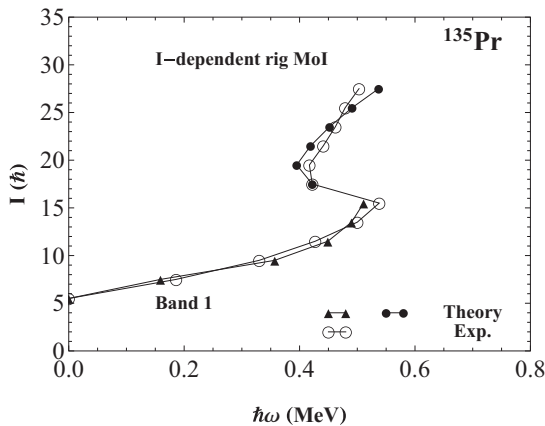


FIG. 19. Comparison between theory and experimental data in the backbending plot for band 1. Theoretical values are shown by solid triangles for  $I \leq 31/2$  and by solid circles for  $I \geq 35/2$ . Experimental values are shown by open circles. Solid circles are normalized at  $I = 35/2$ .

- [1] A. Bohr and B. R. Mottelson, *Nuclear Structure* (Benjamin, Reading, MA, 1975), Vol. II, Chap. 4.
- [2] S. W. Ødegård, G. B. Hagemann, D. R. Jensen, M. Bergström, B. Herskind, G. Sletten, S. Törmänen, J. N. Wilson, P. O. Tjøm, I. Hamamoto, K. Spohr, H. Hübel, A. Görge, G. Schönwäßer, A. Bracco, S. Leoni, A. Maj, C. M. Petrache, P. Bednarczyk, and D. Curien, *Phys. Rev. Lett.* **86**, 5866 (2001).
- [3] D. R. Jensen, G. B. Hagemann, I. Hamamoto, S. W. Ødegård, B. Herskind, G. Sletten, J. N. Wilson, K. Spohr, H. Hübel, P. Bringel, A. Neußer, G. Schönwäßer, A. K. Singh, W. C. Ma, H. Amro, A. Bracco, S. Leoni, G. Benzoni, A. Maj, C. M. Petrache, G. LoBianco, P. Bednarczyk, and D. Curien, *Phys. Rev. Lett.* **89**, 142503 (2002).
- [4] D. R. Jensen *et al.*, *Nucl. Phys. A* **703**, 3 (2002).
- [5] A. Görge, R. M. Clark, M. Cromaz, P. Fallon, G. B. Hagemann, H. Hübel, I. Y. Lee, A. O. Macchiavelli, G. Sletten, D. Ward, and R. Bengtsson, *Phys. Rev. C* **69**, 031301(R) (2004).
- [6] G. Schönwäßer *et al.*, *Phys. Lett. B* **552**, 9 (2003).
- [7] H. Amro *et al.*, *Phys. Lett. B* **553**, 197 (2003).
- [8] D. J. Hartley, R. V. F. Janssens, L. L. Riedinger, M. A. Riley, A. Aguilar, M. P. Carpenter, C. J. Chiara, P. Chowdhury, I. G. Darby, U. Garg, Q. A. Ijaz, F. G. Kondev, S. Lakshmi, T. Lauritsen, A. Ludington, W. C. Ma, E. A. McCutchan, S. Mukhopadhyay, R. Pifer, E. P. Seyfried, I. Stefanescu, S. K. Tandel, U. Tandel, J. R. Vanhoy, X. Wang, S. Zhu, I. Hamamoto, and S. Frauendorf, *Phys. Rev. C* **80**, 041304(R) (2009).
- [9] K. Tanabe and K. Sugawara-Tanabe, *Phys. Rev. C* **73**, 034305 (2006); **75**, 059903(E) (2007).
- [10] K. Tanabe and K. Sugawara-Tanabe, *Phys. Rev. C* **77**, 064318 (2008).
- [11] K. Sugawara-Tanabe and K. Tanabe, *Phys. Rev. C* **82**, 051303(R) (2010).
- [12] K. Sugawara-Tanabe, K. Tanabe, and N. Yoshinaga, *Prog. Theor. Exp. Phys.* (2014) 063D01.
- [13] J. T. Matta, U. Garg, W. Li, S. Frauendorf, A. D. Ayangeakaa, D. Patel, K. W. Schlax, R. Palit, S. Saha, J. Sethi, T. Trivedi, S. S. Ghugre, R. Raut, A. K. Sinha, R. V. F. Janssens, S. Zhu, M. P. Carpenter, T. Lauritsen, D. Seweryniak, C. J. Chiara, F. G. Kondev, D. J. Hartley, C. M. Petrache, S. Mukhopadhyay, D. V. Lakshmi, M. K. Raju, P. V. Madhusudhana Rao, S. K. Tandel, S. Ray, and F. Donau, *Phys. Rev. Lett.* **114**, 082501 (2015).
- [14] S. Frauendorf and F. Döna, *Phys. Rev. C* **89**, 014322 (2014).
- [15] L. D. Landau and E. M. Lifshitz, *Mechanics* (Physics-Mathematics Institute, Moscow, 1958), Sec. 37.
- [16] S. G. Nilsson, *Dan. Mat. Fys. Medd. Vid. Selsk.* **29**, no. 16 (1955).
- [17] K. Tanabe and K. Sugawara-Tanabe, *Phys. Lett. B* **34**, 575 (1971).
- [18] K. Tanabe and K. Sugawara-Tanabe, *Phys. Rev. C* **91**, 034328 (2015).
- [19] R. Garg, S. Kumar, M. Saxena, S. Goyal, D. Siwal, S. Kalkal, S. Verma, R. Singh, S. C. Pancholi, R. Palit, D. Choudhury, S. S. Ghugre, G. Mukherjee, R. Kumar, R. P. Singh, S. Muralithar, R. K. Bhowmik, and S. Mandal, *Phys. Rev. C* **92**, 054325 (2015).
- [20] A. Bohr, *Mat. Fys. Medd. Dan. Vid. Selsk.* **26**, no. 14 (1952).
- [21] K. Tanabe and K. Sugawara-Tanabe, *Phys. Rev. C* **19**, 552 (1979). In the left-hand side of Eq. (6c),  $U_{j_X} U^{-1}$  should read  $U_{j_X} U^{-1}$ , and in the left-hand side of Eq. (8),  $R_X$ ,  $R_Y$ , and  $R_Z$  should read  $R_x$ ,  $R_y$ , and  $R_z$ .
- [22] I. Hamamoto, *Phys. Rev. C* **65**, 044305 (2002).
- [23] D. Bengtsson and J. Helgessen, Lecture notes from a summer school at Oak Ridge, 1991 (unpublished).
- [24] B. Banerjee, H. J. Mang, and P. Ring, *Nucl. Phys. A* **215**, 366 (1973).
- [25] K. Tanabe and K. Sugawara-Tanabe, *Prog. Theor. Phys.* **83**, 1148 (1990).
- [26] K. Tanabe and K. Sugawara-Tanabe, *Phys. Lett. B* **259**, 12 (1991).
- [27] E. Grosse, F. S. Stephens, and R. M. Diamond, *Phys. Rev. Lett.* **31**, 840 (1973).
- [28] E. Grosse, F. S. Stephens, and R. M. Diamond, *Phys. Rev. Lett.* **32**, 74 (1974).
- [29] F. S. Stephens, *Rev. Mod. Phys.* **47**, 43 (1975).